Geosystems and Geoenvironment 2 (2023) 100112

Contents lists available at ScienceDirect

Geosystems and Geoenvironment

journal homepage: www.elsevier.com/locate/geogeo

# Assessment of reservoir stress state and its implications for Paleozoic tight oil reservoir development in the Oued Mya Basin, northeastern Algerian Sahara

Rafik Baouche[a], Shib Sankar Ganguli[b,*], Souvik Sen[c], Ahmed E. Radwan[d]

[a] Department of Geophysic, Laboratory of Resources Minérals at Energétiques, Faculty of Hydrocarbons and Chemistry (FHC), University M'Hamed Bougara Boumerdes, Boumerdès 35000, Algeria
[b] Marine & Deep Seismics Research Group, CSIR-National Geophysical Research Institute, Uppal Road, Hyderabad 500007, Telangana State, India
[c] Geologix Limited, Dynasty Building, Andheri Kurla Road, Andheri (E), Mumbai 400059, Maharashtra, India
[d] Faculty of Geography and Geology, Institute of Geological Sciences, Jagiellonian University, Gronostajowa 3a, 30-387, Kraków, Poland

ARTICLE INFO

*Article history:*
Received 8 March 2022
Revised 30 June 2022
Accepted 26 July 2022

Handling Editor: Yirang Jang

*Keywords:*
In-situ stresses
Multiple linear regression
Image logs
Cambrian reservoir
Ordovician reservoir
Oued Mya Basin

ABSTRACT

The Cambrian and Ordovician clastic reservoirs of the Oued Mya Basin exhibit significant vertical thickness and extensive lateral continuity, despite being tight. These reservoir intervals have not been properly understood yet in terms of in-situ stress distribution and pore pressure behaviour. The main objectives were to infer the reservoir stress state and draw implications for the tight oil reservoir development based on the geomechanical analyses. We interpreted breakouts from a cumulative 1485 m of acoustic image logs and interpreted a NW-SE $S_{HMax}$ orientation (N125°E-N147°E) in the Oued Mya Basin. The inferred breakouts were of B-D quality as per the World Stress Map ranking criteria. Both the reservoirs have a pore pressure gradient of 13.58-13.77 MPa/km, while the minifrac data infers a reservoir $S_{hmin}$ gradient of 17.3-19.2 MPa/km. Based on the breakout widths, we estimated the $S_{HMax}$ gradient as 23.8-26.5 MPa/km. Following the univariate regression analyses to identify various influencing parameters on horizontal stress magnitudes, we proposed multiple linear regression (MLR) models to predict the $S_{hmin}$ and $S_{HMax}$ based on pore pressure, $S_v$, Poisson's ratio, and Young's modulus. Results indicate that $S_v$ influences the horizontal stress estimates significantly more as compared to the other influencing variables. The predicted $S_{hmin}$ and $S_{HMax}$ values are in good agreement (goodness of fit as $R^2$ = 0.976 and 0.994) with the measured data. The newly proposed MLR equations can be utilized in absence of subsurface validation data. A strike-slip faulting reservoir stress state is concluded from stress polygon analysis. An optimum drilling strategy is discussed based on the observed wellbore failures. We recommended the drilling fluid pressure to be increased by 8 MPa and 14 MPa to avoid breakouts against the Ordovician and Cambrian reservoirs respectively, however, that may incur tensile fractures which do not have a considerable effect on wellbore stability while drilling. Based on this work, horizontal well trajectory along NE-SW (i.e., parallel to $S_{hmin}$), together with oriented perforations aligned parallel to inferred $S_{HMax}$ direction is recommended. The potential fracture reactivation risks during reservoir pressurization are evaluated and discussed.



## 1. Introduction

Understanding of reservoir stress state has multifaceted applications in hydrocarbon exploration and development. Reservoir geomechanical characterization is crucial in achieving stable wellbore, optimum drilling, ideal horizontal well trajectories, perforation direction, stimulation, and completion schemes, which greatly impacts the reservoir production (Zoback, 2007; Tingay et al., 2009; Zhang, 2013; Busetti and Reches, 2014; Rajabi et al., 2016; Ju et al., 2017; Liang et al., 2018; Ganguli and Sen, 2020; Lund Snee and Zoback, 2020; Radwan and Sen, 2021a). This is also critical for the later stages of field development where the primary challenges are faced due to the reservoir depletion and necessary repressurization by water injection to maintain production targets as well as caprock integrity (Taghipour et al., 2019; Kaseem et al., 2021;

* Corresponding author.
*E-mail address:* shibg@ngri.res.in (S.S. Ganguli).

https://doi.org/10.1016/j.geogeo.2022.100112

Radwan and Sen, 2021b). In practice, the World Stress Map (WSM) provides key insights into the regional stress field; however, little information about the stress state at the reservoir or local scale can be obtained. For this, estimation of in situ stress state in petroleum basins becomes crucial, which may augment useful information for the WSM project as well.

Various researchers have worked on the in-situ stress analysis of Ghadames (Berkine) Basin, Ahnet Basin, Hassi Messaoud area, Bhiret Hammou, southeastern Constantine field, Illizi and Tiguentourine hydrocarbon fields of Algeria using petroleum data set (McGowen et al., 1996; Koceir and Tiab, 2000; Patton et al., 2003; English et al., 2017; Paludan et al., 2017; Baouche et al., 2020a, 2020b, 2020c, 2021a, 2021b, 2021c), and interpreted a strike-slip faulting stress state with NW-SE oriented maximum horizontal stress in the Algerian platform. Along with the Berkine and Illizi basins, Oued Mya has been a very prolific basin, producing principally from the Paleozoic reservoirs (Benamrane et al., 1993; Benayad et al., 2011). Sonatrach, the Algerian national oil company has thoroughly investigated to document unknowns from this basin and made a promising discovery from the Triassic intervals with its Oued Noumer Sud 1 (ONRS-1) exploratory well, drilled in the Zelfana exploration block in June 2016. Moreover, a huge amount of unexploited hydrocarbon reserves has been discovered recently from the Hassi Berkine, Bir Berkine, and other nearby fields (Galeazzi et al., 2010). This has renewed expectations of petroleum play within the under-explored northern parts of the basin, and the exploration and development campaign is expected to intensify in the Oued Mya Basin. Hitherto, there has been no prior geomechanical work reported from the Oued Mya Basin that provides an excellent prospect to examine the reservoir's in-situ stress state utilizing the high-quality geophysical logs from the recently drilled wells.

The primary objective of this work was to infer the in-situ stress state of the Paleozoic reservoirs from the Oued Mya Basin by integrating wireline logs, drilling data, core data, and various subsurface measurements from eleven vertical wells. These reservoir intervals are identified with poor porosity (dominantly <8%) and permeability <1 mD, a typical representative of tight formation. We presented a petrophysical analysis to understand the fluid flow and storage potential of the studied reservoirs. The geomechanical characterization reported here yields the magnitude of pore pressure, three principal stresses, i.e., vertical stress ($S_v$), least ($S_{hmin}$), and maximum horizontal stress ($S_{HMax}$) magnitudes. The $S_{HMax}$ magnitude and orientation are inferred from the wellbore compressive failures as observed in the acoustic image logs. In practice, the availability of direct calibration data for $S_{hmin}$ and $S_{HMax}$ is scarce. To address this, we adopted univariate regression models to understand and identify various influencing parameters such as vertical stress, pore pressure, Poisson's ratio, and Young's modulus on the horizontal stress magnitudes. Finally, suitable models using the multiple linear regression method have been proposed to predict the $S_{hmin}$ and $S_{HMax}$ magnitudes based on influencing variables. To evaluate the prediction performances of these developed models, we compared the outputs with the $S_{HMax}$ values obtained from breakout widths using image logs. We have also discussed the model limitations and associated uncertainties due to the lack of sufficient downhole calibration data as well as core measurements. Based on the analysis, we presented a comprehensive resource development strategy that focused on achieving wellbore stability during drilling as well as stimulation optimization and associated fracture reactivation risks.

## 2. Regional geological setting

The Oued Mya Basin is an elongated Paleozoic cratonic depression in the northeastern Algerian Saharan platform. The basin is bounded by the Hassi Messaoud Arch and Amguid Arch in the east, Allal High, Tilrhemt High, and Idjerane Arch in the west (Fig. 1). Touggourt saddle is situated in the north, while a structural terrace separates the Oued Mya Basin from the Mouydir Basin in the south. The basin has witnessed multiple compression and extension phases of the Pan-African (590 Ma) as well as Alpine orogeny (65 Ma; Benayad et al., 2011). The basin is characterized by vertical N-S, NNE, and NNW-oriented Pan-African basement faults (English et al., 2017). The long-lived vertical strike-slip faults have been reactivated multiple times during the geological evolution through the transtensional and transpressional episodes (Galeazzi et al., 2010). The basin hosts a cumulative of 4500-5000 m of sedimentary succession (Benamrane et al., 1993; Yahi and Khatir, 1995). Most of the oil and gas accumulations in the Oued Mya Basin are located on the low-relief structures along the flank of the Tilrhemt Arch (Klett, 2000). Researchers have interpreted that these accumulations are majorly within the anticlines, faulted anticlines, or fault blocks developed during the Hercynian and Austrian deformation (Petroconsultants, 1996; Boote et al., 1998; Klett, 2000). A regional lithostratigraphic section is provided in Fig. 2 (Klett, 2000). Primary hydrocarbon reservoirs of the Oued Mya Basin belong to the R1 sandstones and Hamra Quartzites of the Cambrian and Ordovician ages respectively (Benayad et al., 2011). The Cambrian reservoirs correspond to braided fluvial units being unconformably deposited above the pre-Cambrian metamorphic basement (Carr, 2002; Lang et al., 2012). This was followed by the deposition of the Early Paleozoic transgressive shales, namely El Gassi Shale, which separates the Cambrian reservoir from the glaciogenic Ordovician reservoir. The base of the Ordovician Hamra quartzite Formation marks a sequence boundary between preglacial and glacial deposits. Benayad et al. (2013, 2014) studied the petrographic characteristics of the Ordovician reservoirs and inferred that the principal diagenetic factors controlling the reservoir quality are quartz overgrowths and pore-filling illites which reduced the reservoir porosity and permeability. Chlorites have been reported within the Cambrian reservoirs produced by the illite transformation. The post-glacial sea-level increase deposited organic-rich marine shales during Silurian (McDougall et al., 2003; Eschard et al., 2005). Both the Lower Silurian and Ordovician shales are the established source rocks, with high total organic carbon content (~6%-14%; Benamrane et al., 1993). The Jurassic evaporites formed the regional seal to the petroleum system.

**Table 1**
Locations of the studied wells

| Well name | Latitude | Longitude |
|---|---|---|
| Well-A | 32° 17' 13.36" N | 5° 29' 35.20" E |
| Well-B | 32° 21' 23.33" N | 5° 45' 01.29" E |
| Well-C | 32° 22' 29.17" N | 6° 15' 02.37" E |
| Well-D | 32° 12' 31.45" N | 5° 59' 00.14" E |
| Well-E | 32° 08' 11.24" N | 5° 28' 55.41" E |
| Well-F | 31° 59' 05.44" N | 5° 45' 21.38" E |
| Well-G | 31° 45' 57.32" N | 6° 10' 55.46" E |
| Well-H | 32° 04' 29.10" N | 6° 30' 12.33" E |
| Well-I | 31° 29' 38.43" N | 5° 21' 01.25" E |
| Well-J | 31° 30' 15.19" N | 5° 43' 09.55" E |
| Well-K | 31° 18' 51.32" N | 6° 02' 10.47" E |

Refer to Fig. 1

## 3. Data

This work investigates eleven vertical wells. Due to the data sharing restrictions, we could not reveal the actual well names and therefore in this paper, we referred to those as Well-A to Well-K. The well locations are presented in Table 1 and plotted in Fig. 1. All the wells were drilled through the Cambrian reservoir. Routine

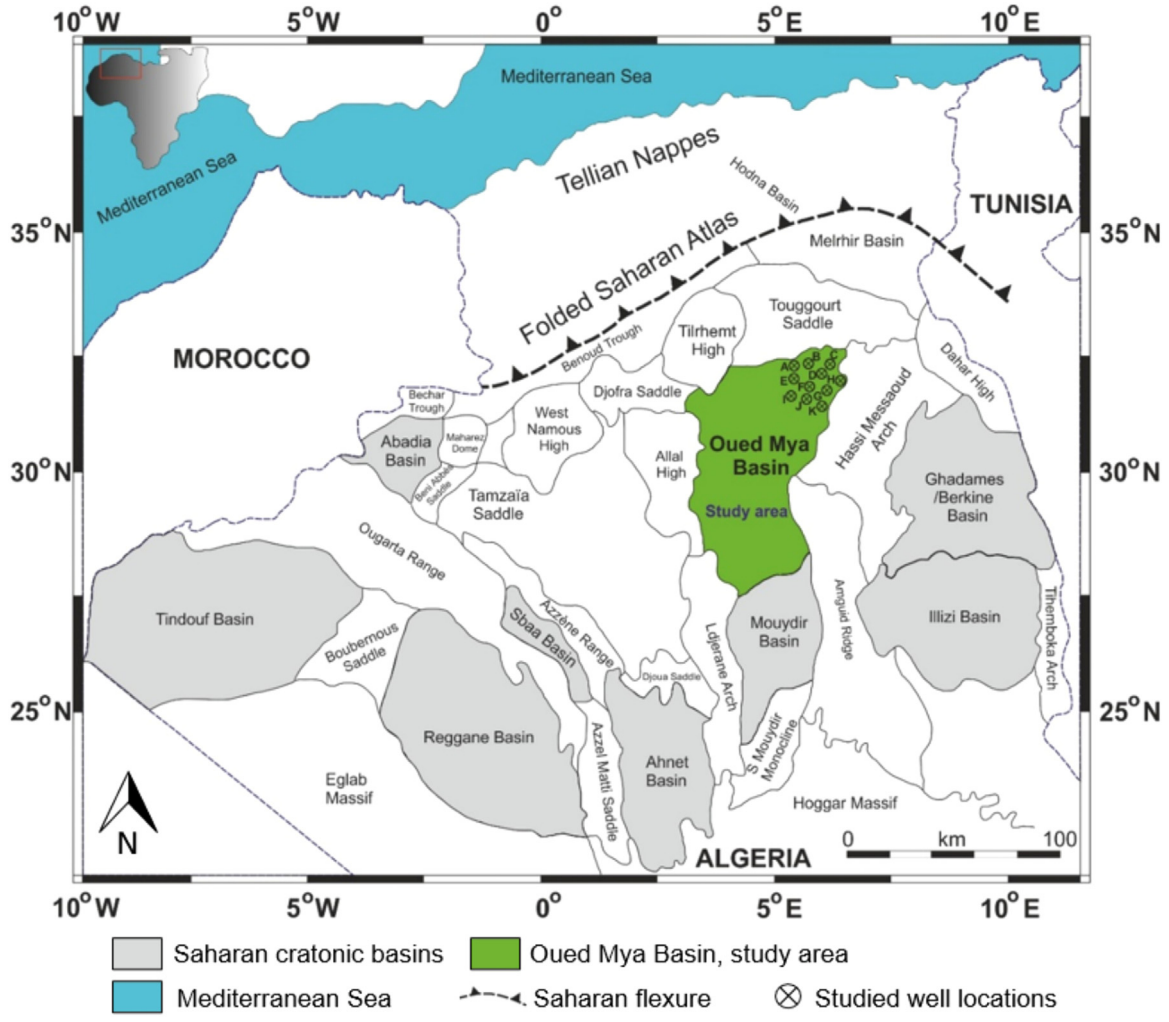


**Fig. 1.** Location map of the Oued Mya Basin situated at the northeastern Algerian Saharan platform, together with the nearby basins, structural features, and studied well locations. The base map is adapted from KeyFacts Energy (2016).

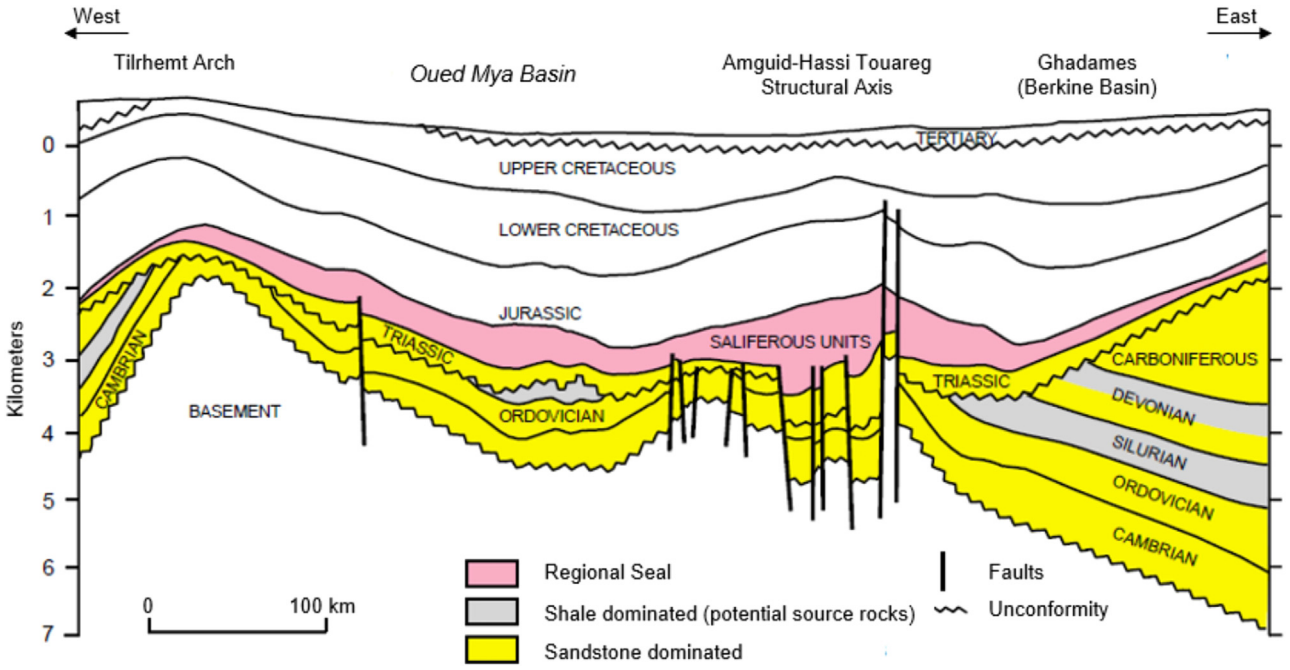


**Fig. 2.** Representation of a regional lithostratigraphic section of the Oued Mya Basin (Klett, 2000).

core analysis (RCA) was accomplished on the core samples covering reservoir pay zones, as obtained from the four studied wells (Well-B, E, F, and I). Wireline geophysical logs were recorded in all the wells, which were the primary input parameters in the geomechanical analyses. Six wells (Well-A, C, D, E, G, and K) had acoustic image log data set. Downhole measurements of formation pressure and minifrac were available from one well (Well-K), used for the calibration and validation of various calculated parameters.

## 4. Methodologies and workflows

### 4.1. Reservoir characterization

Regionally, the extent of both the reservoirs was inferred based on the well log-based correlations. Conventional cores were taken out from the reservoir intervals of four wells, each of which has a diameter of about 6 inches. RCA was performed on the core plug samples, which provided 244 data points comprising grain density, porosity obtained by helium porosimeter, and horizontal permeability measured by permeameter. Briefly, the reservoir petrophysical properties were estimated to understand the reservoir flow potential and storage capacity. For this, we employed the methodology given by Amaefule et al. (1993), which weighs the reservoir quality index (RQI) and flow zone indicator (FZI) based on porosity and permeability measurements (Nabawy et al., 2018; Abuamarah et al., 2019; Abuamarah and Nabawy, 2021). Utilizing the spectral gamma-ray data (Thorium and Potassium concentration), we inferred the possible clay minerals associated with the reservoir facies (Klaja and Dudek, 2016; De et al., 2020).

### 4.2. Orientation of the horizontal stress components

Wellbore breakouts (BO) are one of the important sources of stress orientations (Heidbach et al., 2018). Analyzing image logs is crucial to obtaining meaningful information about borehole failures, within which breakouts emerge as two parallel furrows (failure zones) having 180° angle from each other and parallel to $S_{hmin}$ azimuth (Barton and Moos, 2010; Tingay et al., 2010; Paludan et al., 2017). The acoustic image logs were made available from the studied field using CBIL (Circumferential Borehole Image Log) and UBI (Ultrasonic Borehole Imager) tools, respectively. In order to interpret and characterize the compressive failures within the studied image logs, we followed the WSM ranking guidelines (Heidbach et al., 2018).

### 4.3. Estimation of pore pressure and in-situ stresses

Pore pressure ($P_P$) is an important parameter for geomechanical modeling, as it affects the in-situ stresses. In this work, $P_P$ against the Ordovician and Cambrian reservoirs was recognized from the direct downhole measurements using the MDT tool (Modular Dynamic Tester Instrument). These direct formation pressure values are considered to be the most consistent evaluations of pore pressures if the downhole pressure gauges are suitably attuned. We have also included the drilling mud pressure data and well reports to check for any possible fluid influx event during drilling.

Here, we discuss the methods to estimate the magnitudes of three principal stress components – vertical stress, minimum, and maximum horizontal stresses. Vertical or overburden stress ($S_v$) is defined as the sum of pressure exercised by the superimposing lithological column. $S_v$ was computed using the bulk density log, measured along with the depth (Plumb et al., 1991). Since the density log was not recorded in the shallow section of the well, we generated a pseudo-density profile following the Amoco equation to fill the data gap (Baouche et al., 2020b, 2020c):

$$\rho b_{extrapolated} = \rho b_{surface} + \left(\frac{TVD}{3125}\right)^{cf} \quad (1)$$

where, $\rho b_{extrapolated}$ is the extrapolated density from the surface, $\rho b_{surface}$ is the surface sediment density, 'TVD' stands for the true vertical depth, 'cf' is the associated correlation factor. Extrapolated density is then matched with the wireline density log at a deeper depth by modifying the fitting parameter (cf) so that it follows the true density trend. A composite density profile was generated by appending the pseudo-density profile with the wireline bulk-density log and the same is utilized to estimate $S_v$. Minimum horizontal stress ($S_{hmin}$) defines the lower bound of the pressure essential to break a formation through a known pore pressure gradient. We have employed Eaton's method to estimate the $S_{hmin}$ magnitude:

$$S_{hmin}Eaton = \frac{\upsilon}{1-\upsilon}(S_v - P_P) + P_P \quad (2)$$

where $\upsilon$ is the dynamic Poisson's ratio, which can be calculated from P and S wave velocities. In the second approach, we have applied Matthews and Kelly's (1967) method to generate the $S_{hmin}$ profile against the reservoir. This method relies on the effective minimum horizontal stress ratio interpreted from downhole measurements like leak-off test (LOT), minifrac, etc. The equation is as below:

$$S_{hmin}MK = k\,(S_v - P_P) + P_P \quad (3)$$

where 'k' is the effective minimum horizontal stress ratio. Utilizing the fracture closure pressure (FCP) of mini-frac record, 'k' is determined by:

$$k = \frac{FCP - P_P}{S_v - P_P}. \quad (4)$$

Researchers have suggested utilizing the wellbore breakout width ($W_{BO}$) to estimate the $S_{HMax}$ magnitude (Barton et al., 1988; Zoback, 2007; Lai et al., 2018). In general, breakouts occur along the $S_{hmin}$ direction when the maximum hoop stress (perpendicular to the $S_{HMax}$ orientation) surpasses the rock strength. The following equation can be employed to estimate the $S_{HMax}$ magnitude from borehole compressive failures (Barton et al., 1988):

$$S_{HMax} = \frac{(UCS + 2P_P + \Delta P_P) - S_{hmin}(1 + 2\,Cos\,(\pi - W_{BO}))}{1 - 2Cos(\pi - W_{BO})} \quad (5)$$

where UCS is the uniaxial compressive strength of the formation. Core-based UCS measurements were unavailable, so we estimated it from the compressional sonic slowness log (Freyburg, 1972; Zoback, 2007). Eq. (5) is effective for the case where breakouts are available from image logs. To estimate the $S_{HMax}$ magnitude in the entire reservoir section, various researchers have considered the poroelastic horizontal strain model (Liu and Harpalani, 2014; Gholami et al., 2014; Javani et al., 2017; Najibi et al., 2017; Ganguli and Sen, 2020; Sohail et al., 2020) that involves the static Poisson's ratio ($\upsilon$) and Young's modulus (E), which is given below:

$$S_{HMax} = \frac{\upsilon}{1-\upsilon}(S_v - P_P) + P_P + \frac{E}{1-\upsilon^2}(\upsilon\,\varepsilon x + \varepsilon y) \quad (6)$$

The two strain elements, namely $\varepsilon x$ and $\varepsilon y$ were considered to be mutually perpendicular on a horizontal plane and these are expressed as (Javani et al., 2017; Najibi et al., 2017):

$$\varepsilon x = S_v \frac{\upsilon}{E}\left(\frac{1}{1-\upsilon} - 1\right) \quad (7)$$

$$\varepsilon y = S_v \frac{\upsilon}{E}\left(1 - \frac{\upsilon^2}{1-\upsilon}\right) \quad (8)$$

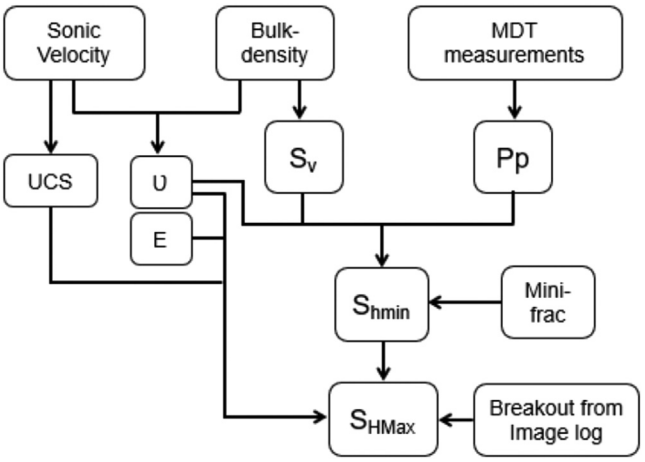


**Fig. 3.** A brief workflow of reservoir pore pressure and in-situ stress analysis using well logs and downhole measurement data, as followed in this work.

In the present study, we have estimated the maximum horizontal stress magnitudes using both approaches. In absence of core-measured static elastic properties, we have employed the dynamic Poisson's ratio and Young's modulus to generate a continuous $S_{Hmax}$ profile by poroelastic approach. The second approach provided $S_{HMax}$ magnitudes based on breakout widths wherever available. A brief workflow of the pore pressure and in-situ stress estimation is presented in Fig. 3. While interpreting the reservoir stress state, we have utilized the stress polygon analysis to constrain the $S_{HMax}$ magnitude ranges. We have also introduced Multiple Linear Regression (MLR) analysis to infer the $S_{hmin}$ and $S_{HMax}$ magnitudes, as discussed later.

## 5. Results

### 5.1. Characteristics of the tight Paleozoic reservoirs

A well-log correlation panel is presented in Fig. 4, which represents the distribution of the Ordovician and Cambrian reservoirs. The Ordovician reservoir is approximately 100-150 m thick, while 200 m+ thickness is encountered in the Cambrian interval. We found that the El Gassi shale splits the two prolific reservoirs and it has increased thickness towards the northern part of the field. Lithofacies and sedimentary structures were inferred from the cored intervals of the Well-F (Fig. 5). In general, the Ordovician interval is characterized by grey to dark grey sandstone (or quartzite) and is devoid of any sedimentary structures (Fig. 5a). These massive sandstones can be formed by suspension fall-out from low- and high-density turbulent flows (Mulder and Alexander, 2001). The considerable thickness of the Ordovician sandstone interval is indicative of sustained turbulent flow (Kneller and Branney, 1995; Stow and Johansson, 2000). The Cambrian sandstones have brownish-grey color and exhibit trough cross-stratification as the dominant sedimentary structure along with minor planar horizontal laminations (Fig. 5b). This is interpreted as three-dimensional dunes deposited from a turbulent high-energy current with steady discharges for longer periods (Mulder and Alexander, 2001). RCA data indicates an average grain density of 2.65

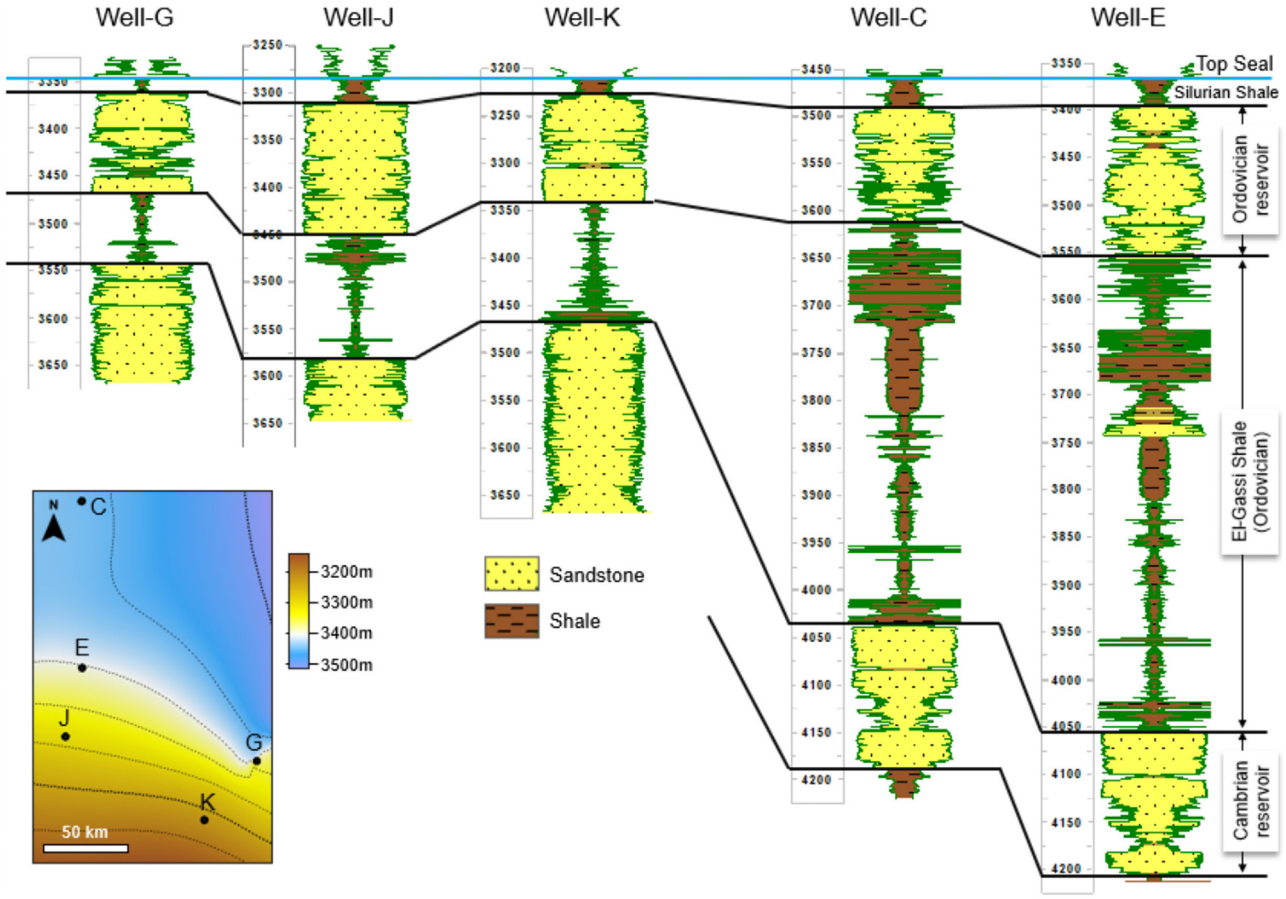


**Fig. 4.** Presents the well-log correlations the Oued Mya field, flattened at the top of the Silurian shale (top seal for the Ordovician reservoir). The map in the inset (left bottom) represents the structural contour map of the Ordovician reservoir top.

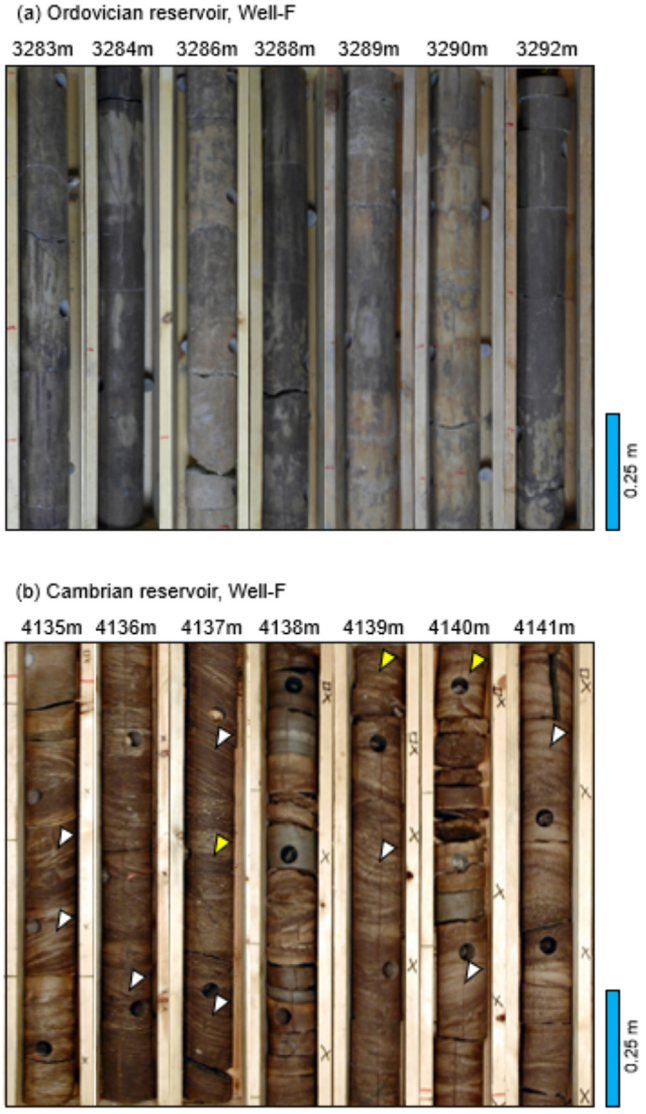


**Fig. 5.** Core photographs of the (a) Ordovician reservoir (3283-3292 m interval) and (b) Cambrian reservoir (4135-4141 m interval) in the Well-F. The Ordovician Formation consists of dark grey sandstones, devoid of any primary sedimentary structure. The Cambrian Formation consists of brownish grey sandstones exhibiting through cross stratifications (marked by white arrows) with minor planar horizontal laminations (marked by yellow arrows). The horizontal fractures seen in the core photographs were created due to the coring technique. The length of each core is 1 m (vertical scale is provided) and the core diameter is about 6 inches (15.24 cm).

gm/cc (Fig. 6a), inferring quartz to be the dominant constituent mineralogy. Both the reservoirs show a 1-12% porosity and 0.01-10 mD permeability range (Fig. 6d), however, the majority of the data points indicate very poor porosity (<6 %; Fig. 6b) and permeability dominantly being <1 mD (Fig. 6c).

The RQI-FZI cross plot (Fig. 6e) indicates that both the reservoirs have RQI < 0.5 µm inferring poor quality, while the FZI varies between 0-10 µm belonging to the poor to good quality variable scale. In the absence of scanning electron microscopy data, Th and K concentrations from spectral gamma-ray logs were useful to infer clay types within both the reservoirs and their respective seals (Fig. 6f). The Cambrian reservoirs have Chlorite as the dominant clay mineral phase, while Illite and mica are present within the Ordovician sandstones. The Silurian shales, acting as a seal to the Ordovician reservoir are Illite dominated and the El Gassi shale exhibits montmorillonite and mixed clay minerals as primary constituents. We summarize that the studied reservoirs are laterally continuous and extensive offering impressive thickness yet tight in nature with 4-6% total porosity and very poor permeability, dominantly ranging between 0.01-1 mD.

### 5.2. Horizontal stress orientations

We interpreted a cumulative 1485 m of acoustic image logs from six different wells (Fig. 7). Out of the six, four wells (Well-E, C, D, and K) had image log coverage of both the reservoirs, while Well-G and Well-A had image logs recorded only against Ordovician and Cambrian intervals, respectively. In total, 68 distinct breakout zones (each having >1 m length) were identified, which contributed to a total BO thickness of 588 m. Based on the BO distribution pattern within the reservoir intervals, we inferred the maximum horizontal stress azimuth ranging between N125°E and N147°E, i.e., dominantly NW-SE regional trend. Following the WSM ranking scheme, these interpreted breakouts have been assigned to B-D quality. The results are summarized in Table 2.

### 5.3. Reservoir pore pressure and in-situ stress magnitudes

The Paleozoic of the Oued Mya Basin hosts primary hydrocarbon reservoirs belonging to the Ordovician and Paleozoic ages. Direct downhole measurements by the MDT tool indicate $P_P$ gradient range of 13.47-13.77 MPa/km against the reservoirs, with an average of 13.58 MPa/km (Fig. 8), which is higher than the hydrostatic pressure gradient. This section is drilled with a 14.71-14.93 MPa/km drilling fluid gradient maintaining a 6-7 MPa overbalance. To fill the density data gap in the shallow section, we generated a pseudo density profile considering a surface sediment density ($\rho b_{surface}$) of 1.8 g/cc and a fitting 'cf' value of 0.6 in Eq. (1). $S_v$ interpreted from the composite density log has an average gradient of 22.38 MPa/km.

The minifrac measurements available from Well-K yielded a fracture closure pressure gradient of 17.30-19.20 MPa/km (Fig. 8). The same has been considered as $S_{hmin}$. Continuous minimum horizontal stress profiles were generated by two approaches. The first approach uses the formation Poisson's ratio ($\upsilon$) as represented by Eq. (2). Both the reservoir intervals have $\upsilon$ = 0.24-0.25, while the El Gassi shale has a $\upsilon$ range of around 0.30-0.31 (Fig. 9). Higher $\upsilon$ values contributed to the higher $S_{hmin}$ in the shale formations. The second approach utilizes an effective minimum horizontal stress ratio (k), which is found to be varying between 0.53-0.64 based on the minifrac data of Well-K. The interpreted reservoir $S_{hmin}$ magnitudes validate well with the lower estimate of minifrac results (Fig. 9).

Further, a UCS range of 95-150 MPa is estimated from the two reservoir formations. A similar UCS range of the Cambro-Ordovician reservoirs is reported by Patton et al. (2003) and English et al. (2017) based on the core measurements from the southeastern Algerian hydrocarbon fields. Extensive borehole breakouts are observed from the acoustic image logs against the reservoirs, and we have utilized Eq. (5) to estimate the $S_{HMax}$ magnitudes. The observed breakouts have a 45°-60° width, which provided a 23.8-26.5 MPa/km $S_{HMax}$ gradient range in the Paleozoic reservoirs (Fig. 9). A continuous $S_{HMax}$ profile was inferred from the poroelastic horizontal strain model using rock-mechanical properties (Eq. 6), which confirms judiciously the breakout-based estimates.

## 6. Estimation and validation of $S_{hmin}$ and $S_{HMax}$ magnitudes using multiple linear regression

$S_{hmin}$ and $S_{HMax}$ are the two most important horizontal stress components required to understand the in situ stress behaviour of any region. In general, measurements of $S_{hmin}$ magnitude in a field

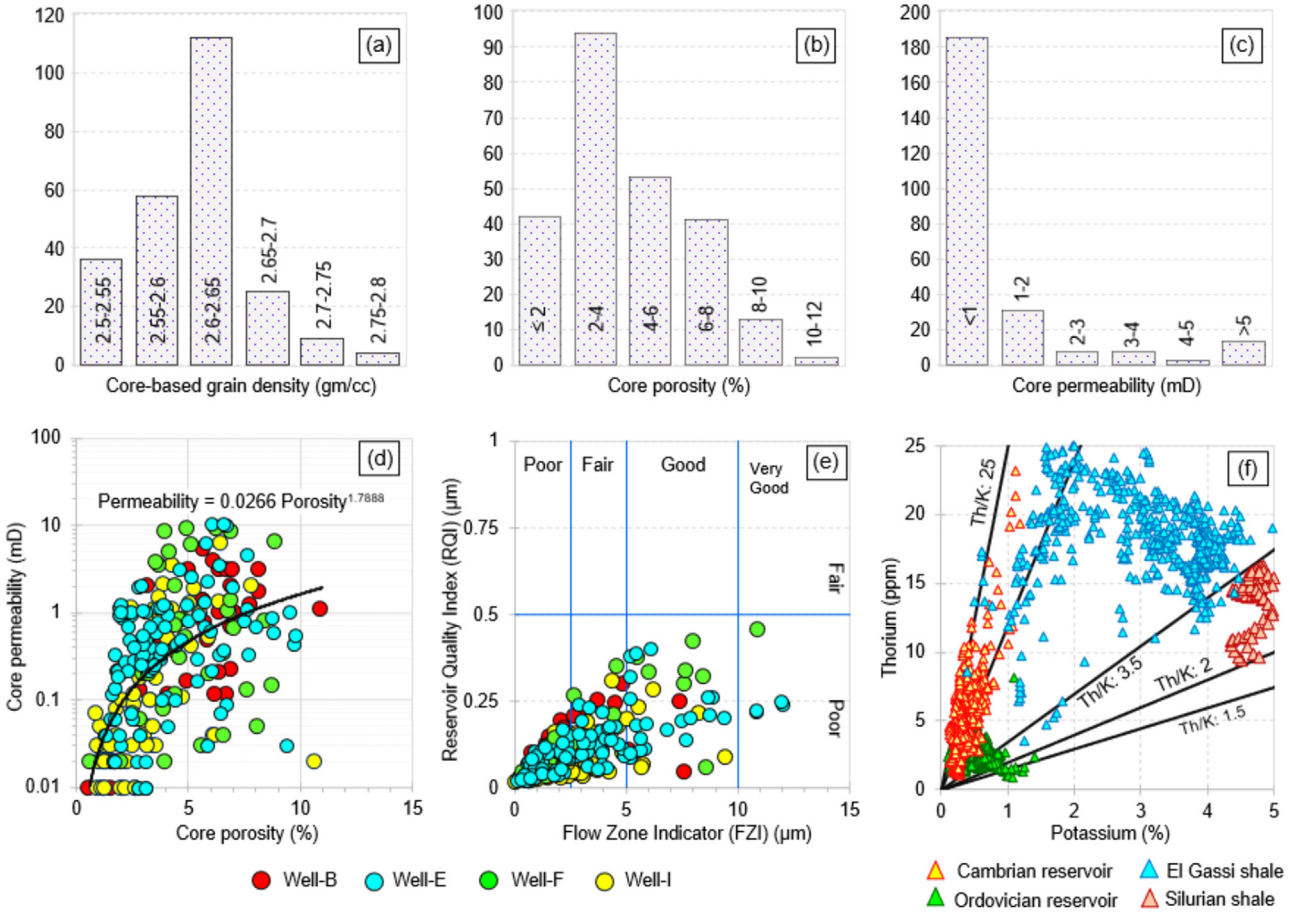


**Fig. 6.** Distribution of core-measured (a) grain density, (b) porosity, and (c) permeability within the Cambrian and Ordovician reservoirs; (d) porosity-permeability relationship, (e) reservoir quality by RQI-FZI cross plot. Core measurements were available in Well-B, E, F, and I. (f) clay mineralogy of the reservoirs and their respective seals inferred from spectral gamma-ray data of Well-H.

**Table 2**
List of acoustic image logs inferred breakouts from each well

| Well Name | Length of Image log | Mean $S_{HMax}$ azimuth | No. of distinct BO Zones | Cumulative BO length | Standard deviation | WSM Quality Ranking | Imaging tool used |
|---|---|---|---|---|---|---|---|
| Well-A | 170m | N125°E | 8 | 90 m | 20° | B | UBI |
| Well-C | 205m | N145°E | 11 | 115 m | 25° | C | CBIL |
| Well-D | 310m | N133°E | 16 | 145 m | 15° | B | UBI |
| Well-E | 410m | N135°E | 20 | 150 m | 17° | B | CBIL |
| Well-G | 80m | N147°E | 6 | 45 m | 33° | D | CBIL |
| Well-K | 310m | N130°E | 7 | 43 m | 14° | B | CBIL |

The table presents the total length of the studied image logs, cumulative count of distinct breakout (BO) zones, total BO length, and the mean $S_{HMax}$ azimuth from the available wells in the Oued Mya Basin. The WSM guidelines were followed for quality ranking.

are not regularly performed within all the wells and that too often restricted to the exploratory phases. Equally important to note that fracture closure pressure (FCP) measured during minifrac tests in the reservoir provides the best estimate of $S_{hmin}$ magnitude. Here, we attempted to estimate the $S_{hmin}$ magnitude using a statistical approach namely multiple regression analyses, as an alternative to the earlier mentioned uniaxial strain model. Out of the 11 studied wells, only 6 directly measured FCP ($S_{hmin}$) values were made available to us for the validation of our results. From a geomechanical point of view, the magnitude of $S_{hmin}$ varies significantly with variables such as $P_P$, $S_v$ and $\upsilon$ (Eq. 2). Keeping these three predictor variables in mind, a multiple linear regression model is developed to evaluate the dependent variable, i.e., $S_{hmin}$ magnitude from the studied region. The statistical analysis incorporates the multivariate analysis of variance (MANOVA) technique to determine whether the means of the groups are unlike. A generalized model of multiple linear regression (MLR) with $Y$ as the dependent variable and $x_i$ as the $i^{th}$ independent variable with i=1,2,3,...., N, can be written in the form of

$$Y = \alpha_0 + \alpha_1 x_1 + \alpha_2 x_2 + \alpha_3 x_3 + .. .. + \alpha_N x_N \quad (9)$$

where $\alpha_0$ is the constant term, intercept and $\alpha_i$ is the coefficient of the $i^{th}$ independent variable $x_i$. The solution for intercept and coefficients can be obtained through the minimization of the sum of squared residuals ($SSR$) of the dependent variable in the form of

$$SSR = \sum_{j=1}^{M} \left(Y_j' - Y_j\right)^2 \quad (10)$$

Here, $Y_j'$ and $Y_j$ are the observed (true) value of the dependent variable and its $j^{th}$ value to be estimated; M is the overall data points of the dependent variable, respectively.

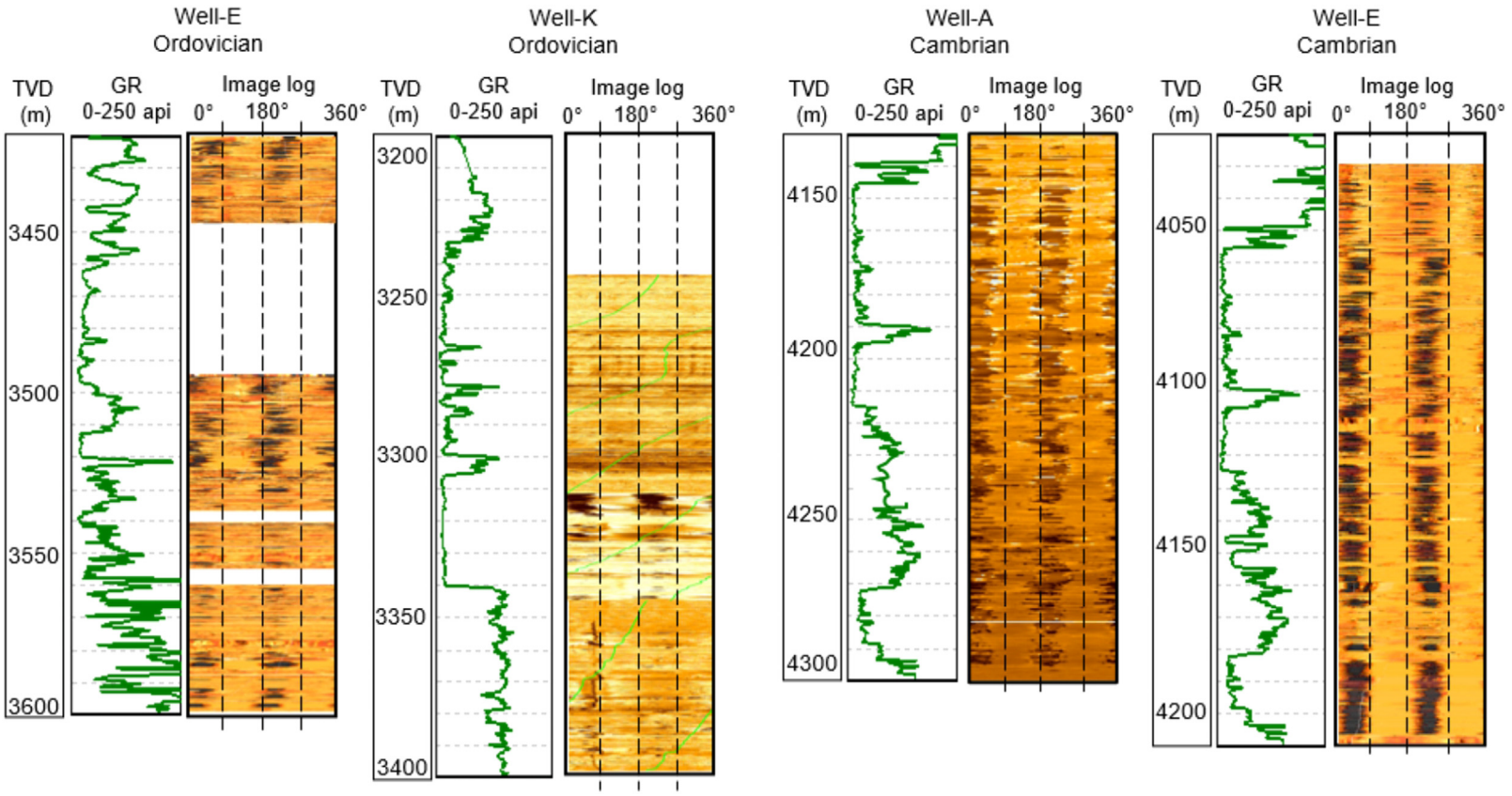


**Fig. 7.** Illustration of acoustic image logs logged through the Ordovician and Cambrian reservoir pay zones. Note that the wellbore breakouts are depicted as two dark coloured parallel furrows (failure zones) that are 180° apart along NE-SW. Gaps within the image logs signify the zones that were not recorded or processed due to poor quality.

**Table 3**
(a) Represents the results from the multiple regression analysis to estimate the $S_{hmin}$ magnitudes from the studied field. (b) Summary of the final model statistics to estimate the $S_{hmin}$ magnitudes from the studied field.

| | | | | | | |
|---|---|---|---|---|---|---|
| (a) | | | | | | |
| ANOVA | | | | | | |
| Model: *MLR* | df | Sum of squares (SS) | Mean square (MS) | F | Significance F | |
| *Dependent variable: FCP** | | | | | | |
| *Predictor variables: $P_P$, Sv, υ* | | | | | | |
| **obtained during mini-frac* | | | | | | |
| Regression | 3 | 117.363 | 39.121 | 28.238 | 0.034 | |
| Residual | 2 | 2.771 | 1.385 | | | |
| Total | 5 | 120.133 | | | | |
| Model Parameters | Coefficients | Standard Error | t Stat | Sig. F | Lower 95% | Upper 95% |
| Intercept (Constant) | -31.442 | 11.301 | -2.782 | 0.108 | -80.067 | 17.182 |
| $S_v$ | -2.512 | 1.28 | -1.962 | 0.188 | -8.020 | 2.995 |
| $P_P$ | 6.60 | 2.421 | 2.726 | 0.112 | -3.815 | 17.016 |
| υ | -70.684 | 75.356 | -0.937 | 0.447 | -394.917 | 253.549 |
| (b) | | | | | | |
| Model | Multiple R | R-Squared ($R^2$) | Adjusted $R^2$ | Standard Error | | |
| MLR | 0.988 | 0.976 | 0.942 | 1.178 | | |

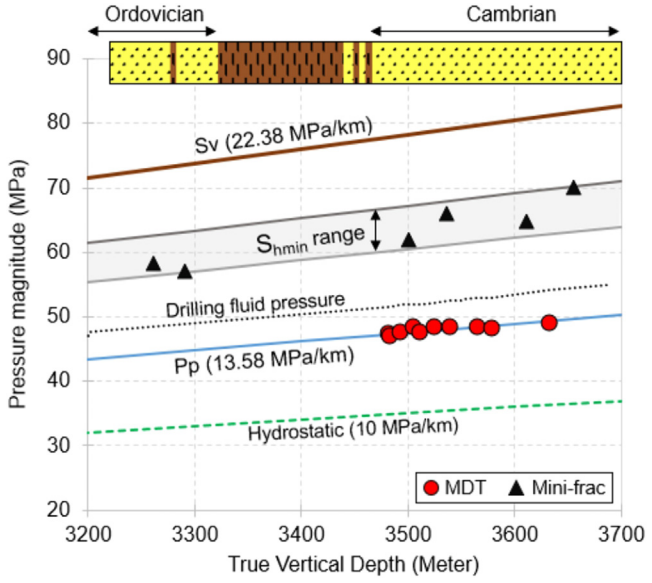


**Fig. 8.** Represents interpreted vertical stress (Sv), pore pressure ($P_P$), and minimum horizontal stress $S_{hmi}$ profiles from the Well K in the Oued Mya Basin. Formation pressure measurements by the MDT tool (red dots) are used to calibrate the $P_P$ profile. Closure pressures from mini-frac tests (black triangles) are used to interpret the estimated $S_{hmi}$ profile.

This method utilizes data to make inferences about the relationship between the predictor (experimental) and dependent variables along with the statistical properties of the entire population. The basic assumptions in this MLR model are: (a) a linear relationship exists between the dependent or outcome variable ($S_{hmin}$) and predictor variables ($P_P$, $S_v$ and υ), (b) the errors between the measured and predicted $S_{hmin}$ values (i.e., residuals) are distributed normally, (c) the variation in the $S_{hmin}$ residuals is constant at each depth point across the model (homoscedasticity), and (d) multicollinearity is absent in the data. Through the MANOVA method, all these assumptions can be verified one by one before concluding the model performance. Further, F-test has been employed to determine the equality of means and compare whether the individual means of the samples are statistically significant or not. A brief flowchart of the MLR modeling workflow is presented in Fig. 10. Null hypothesis testing was done to ensure the outcomes are statistically significant and the data follow the theory that a consequence exists at the population level. Results from the MANOVA method and model summary are shown in Tables 3a and 3b, respectively. The F-statistic ratio (between-groups variance/within-group variance) of the studied data is found to be 28.238, implying that the two variances are not the same across groups. The obtained F-value is quite large enough to reject the null hypothesis. This is justified as the distribution F (3, 2) of this statistical test has a p-value (significance F) of 0.034 (Table 3a), which is much below the evidentiary standard value, i.e., 5% (0.05). In other words, a 3.4% risk has been taken to conclude that the null hypothesis is wrong in this test. This has also been confirmed by the non-zero values of the predicted 95% confidence intervals to define the upper and lower bounds of the model, respectively. Hence, we can infer that the effect is statistically significant at the studied population level. Fig. 11 illustrates the correlation coefficient ($R^2$ = 117.363/120.133) value as 0.976 with a multiple $R^2$ of 0.988 (Table 3b), as obtained from the present multivariate regression analysis. This gives us a reasonable idea of how considerable variability of the magnitude of $S_{hmin}$ is being elucidated by the independent variables, e.g., $P_P$, $S_v$ and υ. The constant intercept (-31.442) is the mean of group means that delivers the $S_{hmin}$ estimates by considering all predictors as zero. The relationship between $S_{hmin}$ and $P_P$, $S_v$ and υ can be written in the form of a linear equation, as given by:

$$S_{hmin} = -2.512S_v + 6.60\,P_P - 70.684\upsilon - 31.442 \quad (11)$$

Similarly, the MANOVA method has been adopted to predict the $S_{HMax}$ magnitude and determine its relationship with all the influencing (independent) variables such as $P_P$, $S_v$, $S_{hmin}$, υ, and $E$ within the Cambrian to Ordovician successions of the Oued Mya Basin. Note that in this case, the independent variables used to estimate the dependent variable ($S_{HMax}$) is more as compared to the prediction of $S_{hmin}$ magnitude. This suggests analyzing several covariates separately and together as well at the same time to find out their relationship (joint and single both) with the outcome. Therefore, apart from multiple linear regression, univariate regression analyses are also performed to find out which parameter or variable is more influential in optimum predictions of $S_{HMax}$ magnitude. As stated earlier, the $S_{HMax}$ magnitudes were inferred from the breakout width observed in the acoustic image logs. Table 4 summarizes the results comprising the relevant equations, goodness of fit ($R^2$), and standard errors from the univariate and multiple regression analyses. The vertical stress data correlates better with the magnitude of $S_{HMax}$ and the correlation of Poisson's ratio is worst when compared with all other influencing variables (Fig. 12). This is strongly evidenced by a relatively higher t-value (refer to t Stat

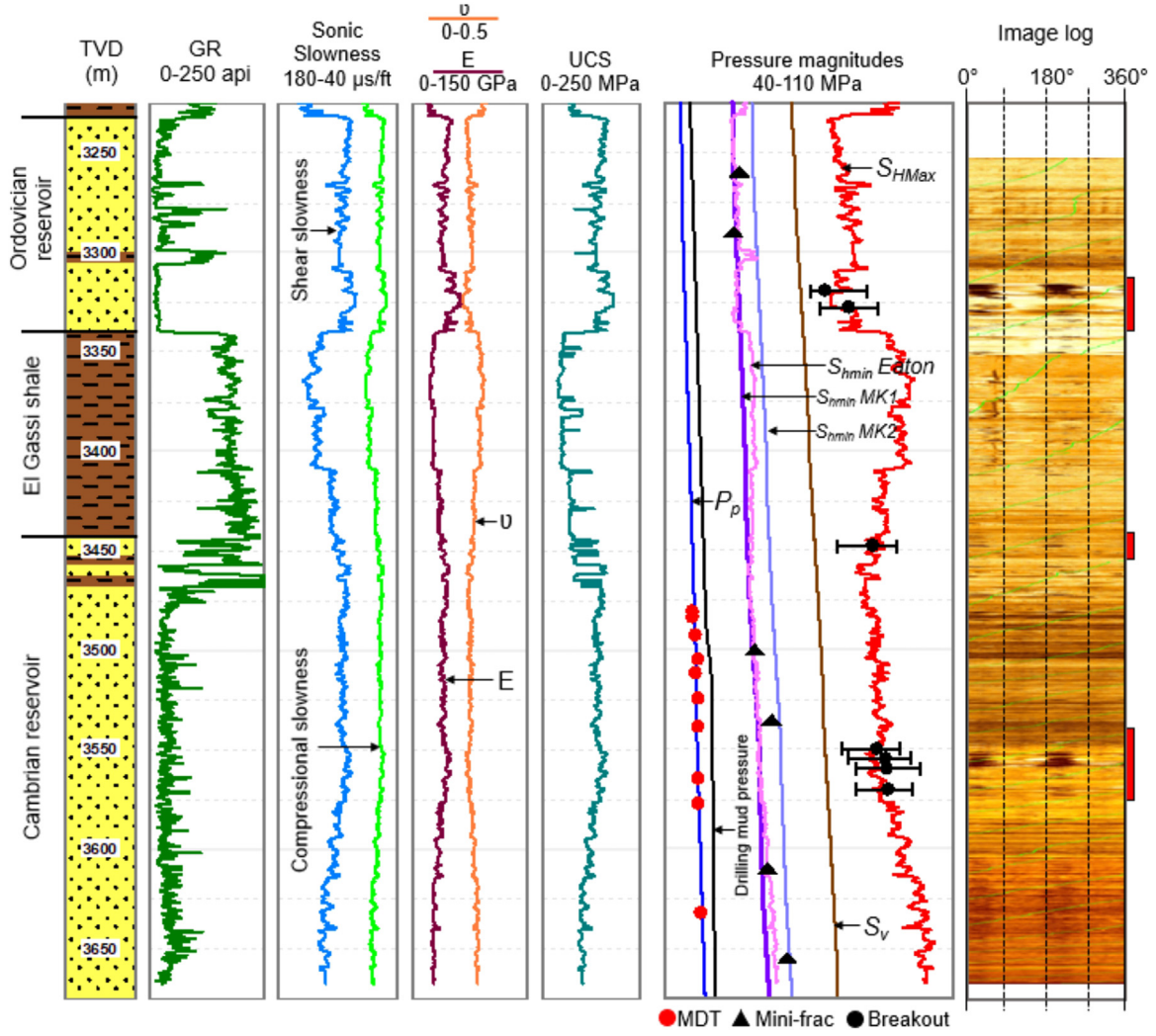


**Fig. 9.** Illustration of the elastic properties, rock strength, pore pressure, and in-situ stress magnitudes from the Well-K of the Oued Mya Basin, along with the acoustic image log. Reservoir $P_P$ is validated with the MDT measurements (red dots on Track 6). '$S_{hmin}$Eaton' is generated by Eaton's method. $S_{hmin}$MK1 and $S_{hmin}$MK2 are generated by Matthews and Kelly (1967) method with an effective minimum horizontal stress ratio (k) of 0.53 and 0.64, respectively. $S_{hmin}$ is validated with minifrac data (black triangles on Track 6). Breakout width-based $S_{HMax}$ magnitude is presented as black dots on Track 6.

**Table 4**
Results from the univariate and multiple regression analyses of variables influencing the SHMax magnitudes.

| | Equation | R-Squared ($R^2$) | Statistical Error |
|---|---|---|---|
| Univariate | $S_{HMax} = 2.132\ S_v$ -75.30 | 0.944 | 0.231 |
| re- | $S_{HMax} = 2.341\ S_{hmin}$ -53.87 | 0.939 | 0.266 |
| gres- | $S_{HMax} = 2.895\ P_P$ - 45.80 | 0.84 | 0.567 |
| sion | $S_{HMax} =$ - 0.521 $E$ +114.11 | 0.242 | 0.412 |
| analyses | $S_{HMax} = 87.77\ \upsilon$ +67.78 | 0.024 | 248.24 |
| Multiple regression analyses (MLR) | $S_{HMax} = 6.06\ S_v + 0.91\ S_{hmin} - 6.45\ P_P + 41.13\ \upsilon + 0.41\ E$ - 163.46 | 0.994 | 0.39 |

Units: $P_P$ (MPa); $S_v$ (MPa), $S_{hmin}$ (MPa), $\upsilon$ (unitless) and $E$ (GPa).

in Table 5) with a significant F value less than 0.05 corresponding to the antecedent $S_v$ as compared to the other variables.

Overall, the multiple regression model performed well with a goodness of fit value of 0.994 and a standard error of 0.39. The ANOVA table, as can be seen in Table 4, recommends the acceptability of the regression model based on a statistical perspective. In this case, the regression row and residual row depict information about the variations considered and rejected by the model, respectively. Note that the distribution F (5, 1) of the population has a p-value (significance F) of 0.041 $<$ 0.05 (allowed standard) with an F-statistic ratio of 333.143. Note that the probability of obtaining a value greater or equal to 333.143 is less than 0.041. Moreover, strong evidence for different means within the groups and between the groups is realized, hence, we can reject the null hypothesis. Fig. 13 demonstrates the goodness of fit and comparison between the multiple regression analysis predicted and true $S_{HMax}$ magnitudes.

In order to predict the $S_{hmin}$ and $S_{HMax}$ stress behaviour within this region, the newly established multiple linear regression models were utilized, as indicated by Eq. (11) and Table 4, respectively. To test the developed model, the predicted values of $S_{HMax}$ are compared with data from other 4 other wells with the measured $S_{HMax}$ values that are not used in the multiple regression analyses. However, we could not test the model for the predic-

**Table 5**
A summary of results from the multiple regression analysis to estimate the SHMax magnitudes from the studied field

| ANOVA | | | | | | |
|---|---|---|---|---|---|---|
| Model: *MLR Dependent variable: BO* Predictor variables: $P_P$, Sv, $S_{hmin}$, $\upsilon$ and E *obtained from image log derived breakout (BO) widths* | df | Sum of squares (SS) | Mean square (MS) | F | Significance F | |
| Regression | 5 | 243.491 | 48.698 | 333.143 | 0.041 | |
| Residual | 1 | 0.146 | 0.146 | | | |
| Total | 6 | 243.637 | | | | |
| Model Parameters | Coefficients | Standard Error | t Stat | Sig. F | Lower 95% | Upper 95% |
| Intercept (Constant) | -163.46 | 22.73 | -7.19 | 0.087 | -452.31 | 125.380 |
| $S_v$ | 6.06 | 1.08 | 5.591 | 0.012 | -7.742 | 19.873 |
| $S_{hmin}$ | 0.91 | 1.04 | 0.873 | 0.541 | -12.307 | 14.125 |
| $P_P$ | - 6.45 | 1.17 | -5.536 | 0.113 | -21.262 | 8.356 |
| $\upsilon$ | 41.13 | 60.81 | 0.676 | 0.621 | -731.58 | 813.844 |
| E | 0.41 | 0.15 | 2.757 | 0.221 | -1.508 | 2.345 |

tions of $S_{hmin}$ variations using Eq. (11) from other wells due to the non-availability of the measured $S_{hmin}$ magnitudes. Fig. 14 demonstrates $S_{HMax}$ results from two wells estimated from MLR. It is noteworthy to mention that the multiple regression analyses derived from newly established equations can be employed for the estimation of $S_{hmin}$ and $S_{HMax}$ values using conventional well logs in this region when FCP and wellbore breakouts are scarce or unavailable.

## 7. Discussions

### 7.1. Inferring the reservoir stress state

Based on the interpreted stress magnitude distributions in the Paleozoic reservoirs of the Oued Mya Basin, we infer that the $S_{HMax}$ has the highest magnitude and $S_{hmin}$ is the least principal stress (Figs. 10 and 14). McGowen et al. (1996) reported a wide range of $S_{hmin}$ gradients (14.7-23.97 MPa/km) in the Cambro-Ordovician reservoirs from the hydro-frac database of the Hassi Messaoud field, situated on the eastern side of the Oued Mya field. English et al. (2017) interpreted a $S_{hmin}$ gradient of 12.1-24.1 MPa/km from the downhole measurements recorded in the Cambrian and Ordovician reservoirs of the Illizi Basin, southeastern Algeria. In a recent work from the hydrocarbon fields in the Central Algerian Sahara, Baouche et al. (2021a) inferred a $S_{hmin}$ gradient of 18.77-19 MPa/km from LOT data. Our minifrac-based results further narrow down the Paleozoic reservoir $S_{hmin}$ gradient as 17.30-19.20 MPa/km. That said, our results are well supported by the observation made from the nearby El Gassi field by Baouche et al. (2021a). Further, we presented the inferred in-situ stresses in the form of a stress polygon which was originally introduced by Zoback (2007). The boundaries of each polygon are defined by a frictional faulting mechanism, and we have considered a frictional coefficient value of 0.6 while defining these boundaries. Fig. 15 represents the same from the Ordovician (Fig. 15a) and Cambrian (Fig. 15b) intervals where minifrac measurements and breakouts were present. Stress polygon plots are helpful to infer a possible $S_{HMax}$ range, which is further constrained by compressive failure criteria. Both the reservoirs are plotted in the strike-slip polygon (Fig. 15). At 3322 m depth, within the Ordovician reservoir of Well-K, stress polygon analysis provides a possible $S_{HMax}$ magnitude ranging between 85 MPa and 104 MPa (Fig. 15a), while the breakout width-based approach quantified the $S_{HMax}$ magnitude as 87 MPa. Likewise, the estimated $S_{HMax}$ for the Cambrian reservoir at a depth of 3560 m is found to be 93 MPa, which falls within the $S_{HMax}$ window of 89-111 MPa, as deciphered from the stress polygon approach. We conclude a $S_{HMax}$ gradient of 23.8-26.5 MPa/km from wellbore compressive failures and the MLR approach. Baouche et al. (2021a) reported a similar $S_{HMax}$ gradient (27-29 MPa/km) in the Paleozoic reservoirs of the El Gassi, El Agreb, and Hassi Messaoud fields of the nearby Berkine Basin. Summarily, both the reservoirs of the Oued Mya Basin exhibit $S_{HMax} > S_v > S_{hmin}$ representing a major strike-slip stress state with maximum horizontal stress aligned along N125°E-N147°E as seen from the compressive failure zones. We observed that the mean $S_{HMax}$ orientations in the Well-A, D, E, and K offer a narrow range of N125°E-N135°E, while the stress azimuth is deflected more in the Well-C (N145°E) and Well-G (N147°E) (Table 2), which are situated on the eastern side, close to the Hassi Messaoud Arch (Fig. 1). This local deflection of $S_{HMax}$ orientation is poorly understood but it may be influenced by third-order stress sources (<100 km) related to local density or stiffness contrasts, e.g., pre-existing faults, variation in large fault geometries (Morley, 2010), etc. The inferred NW-SE stress azimuth in the Paleozoic of the Oued Mya Basin is observed to be parallel with the regional trend (Patton et al., 2003; Baouche et al., 2020a, 2021a; English et al., 2017; Paludan et al., 2017) and the movement direction of the African plate (Di Bucci et al., 2010), which infers that the ridge-push force is the principal contributor to the regional stress field.

### 7.2. Tight oil reservoir development strategy

Both the Paleozoic reservoirs are characterized by poor porosities (dominantly <8%) and tight in nature with <1 mD permeability (Fig. 6). Chlorites and illites, inferred from clay mineralogy analysis (Fig. 6f) might be responsible for reservoir porosity reduction. Similar observations were made by Hirst et al. (2001) from the Devonian tight gas sandstones of the Tiguentourine field, Timimoun Basin, central Algeria. Quartz overgrowth may also be responsible for poor porosity in the Ordovician reservoir Benayad et al., 2013). Fractures are almost absent in cores as well as in the acoustic image logs. Our core-based petrophysical investigation did not

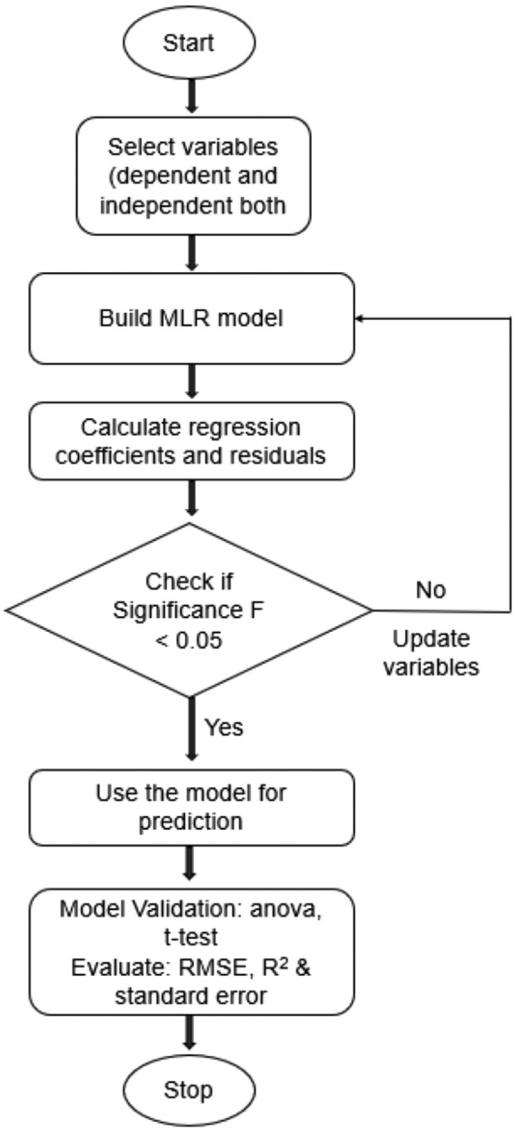


**Fig. 10.** Representation of the flowchart for the MLR model building to generate the minimum ($S_{hmin}$) and maximum horizontal stress ($S_{HMax}$) profiles.

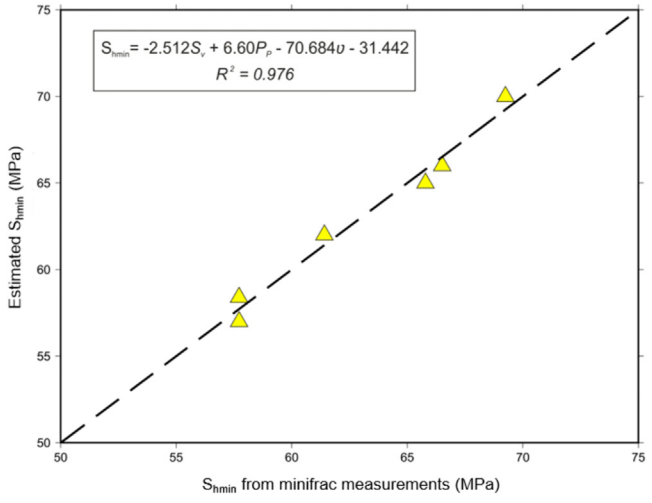


**Fig. 11.** Comparison of the estimated $S_{hmin}$ magnitudes through multiple linear regression and directly measured $S_{hmin}$ values obtained from FCP during hydrofracking. The correlation coefficient is $R^2 = 0.976$.

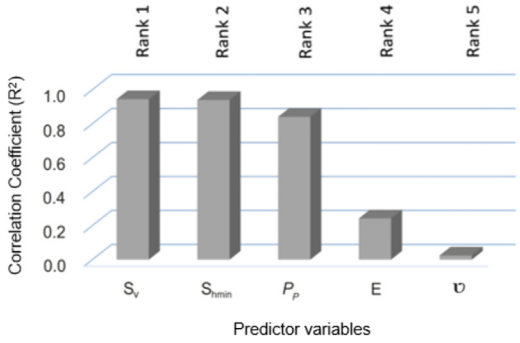


**Fig. 12.** Relative importance (rank wise) of the predictor variables ($P_P$, $S_v$, $S_{hmin}$, $\upsilon$, and $E$) to determine the outcome variable ($S_{HMax}$) based on the correlation coefficient as obtained from the univariate regression analyses.

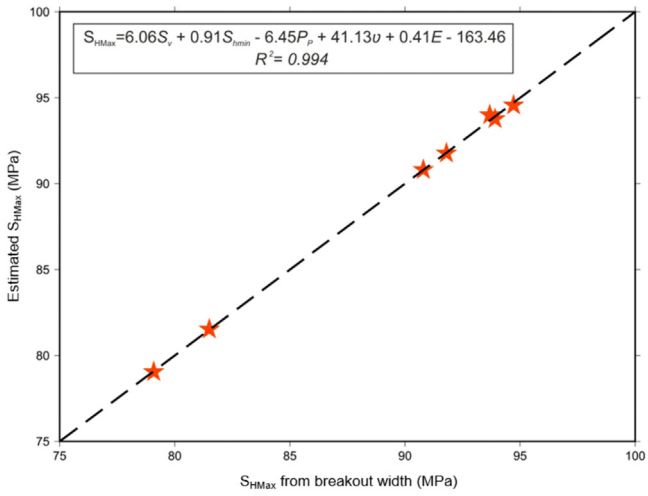


**Fig. 13.** Comparison of the estimated $S_{HMax}$ magnitudes through multiple linear regression and observed $S_{HMax}$ values obtained from breakout width analysis acoustic image log. The goodness of fit is $R^2 = 0.994$.

identify any abnormal or high permeability streaks with the reservoirs which are usually formed by the high concentration of natural fractures and diagenetic alterations (Parvizi et al., 2015). These super permeability flow conduits contribute to the production amplification from a usually tight reservoir interval. In general, both the reservoirs of concern are homogenous and tight. Field correlation indicates that the studied reservoirs are considerably thick with extensive lateral continuity. For reservoir development strategy we focused on two critical aspects – wellbore stability during drilling to minimize the near-wellbore reservoir damage and the necessity of hydraulic fracturing.

### 7.3. Wellbore stability optimization during drilling

Wellbore failures provide critical information on stress orientation, however, these are unwanted while drilling since excessive failure may result in non-productive times as well as abandonment, if uncontrolled. We addressed these instability issues based on the circumferential hoop stress ($\sigma_{\theta\theta}$) concentration concerning the UCS and radial stress ($\sigma_{rr}$) at the borehole wall. Since the rock tensile strength is usually negligible, we have assumed its value as zero in the reservoirs (Lockner, 1995). At a depth of 3520 m within the Ordovician reservoir of Well-E, the in-situ drilling condition with 52 MPa drilling mud pressure indicates $\sigma_{\theta\theta}$ considerably exceeding the reservoir UCS perpendicular to the $S_{HMax}$ direction (Fig. 16a), which yielded NE-SW breakouts in the acoustic image log. Image logs did not reveal any drilling induced tensile fail-

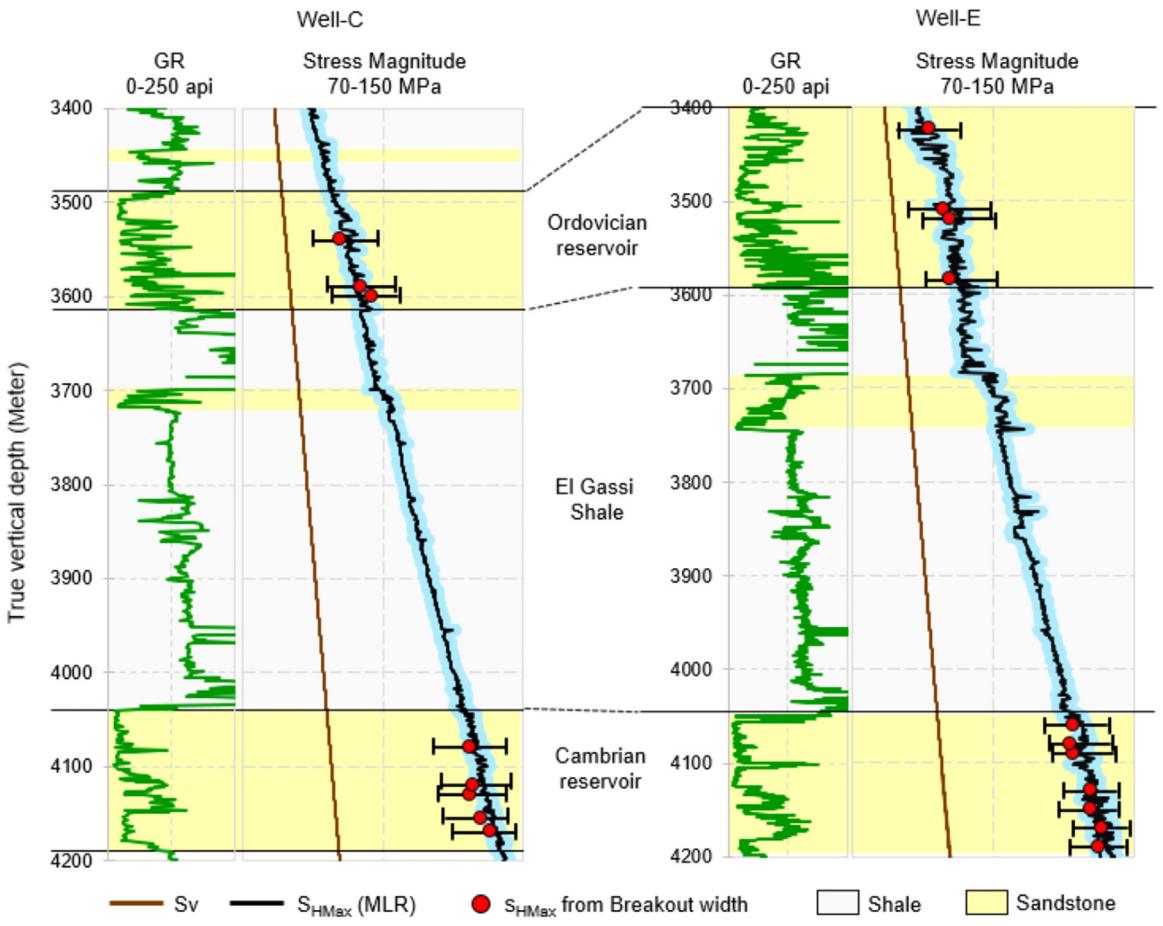


**Fig. 14.** Illustration of the estimated $S_{HMax}$ values using the developed MLR equation (Table 5), together with the measured $S_{HMax}$ obtained from breakout widths and its possible ranges across the Cambrian and Ordovician reservoirs of Well-C and Well-E. The error bar (light blue) denotes the standard deviation of predicted values from the MLR model.

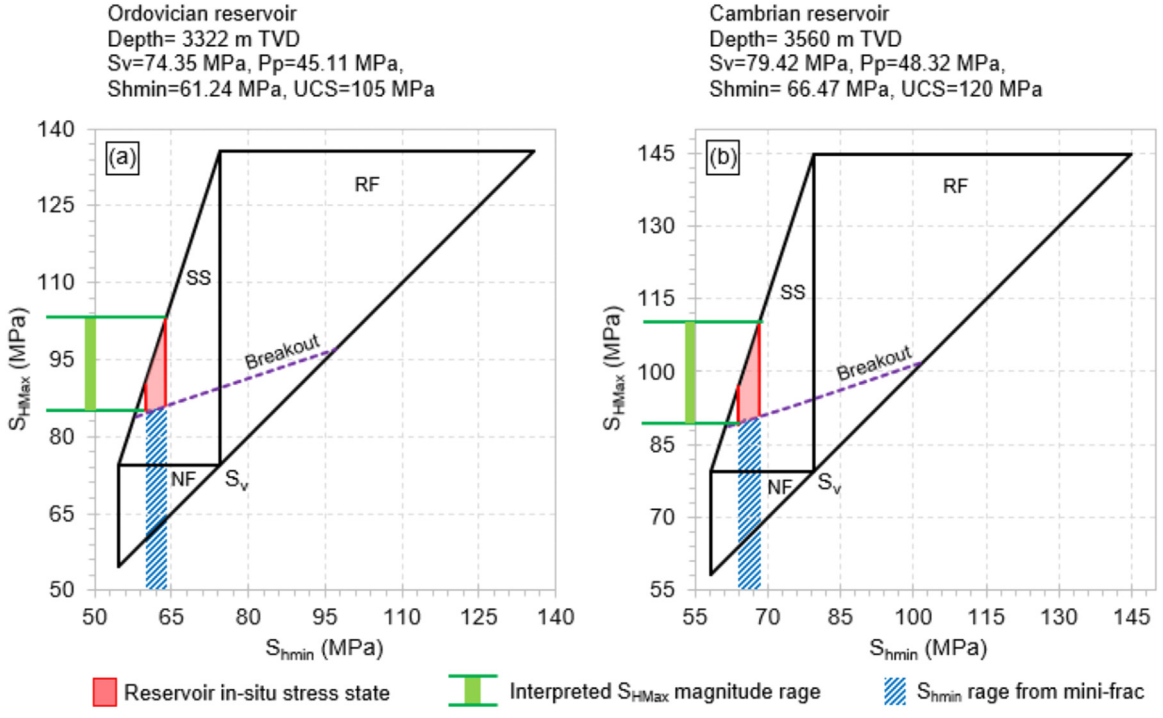


**Fig. 15.** Inferring the stress state by stress polygon plot in (a) Ordovician reservoir (3322 m) and (b) Cambrian reservoir (3560 m) in the Well-K. A possible range of $S_{HMax}$ is inferred based on the breakout criteria (dashed line) and the $S_{hmin}$ range inferred from mini-frac tests.

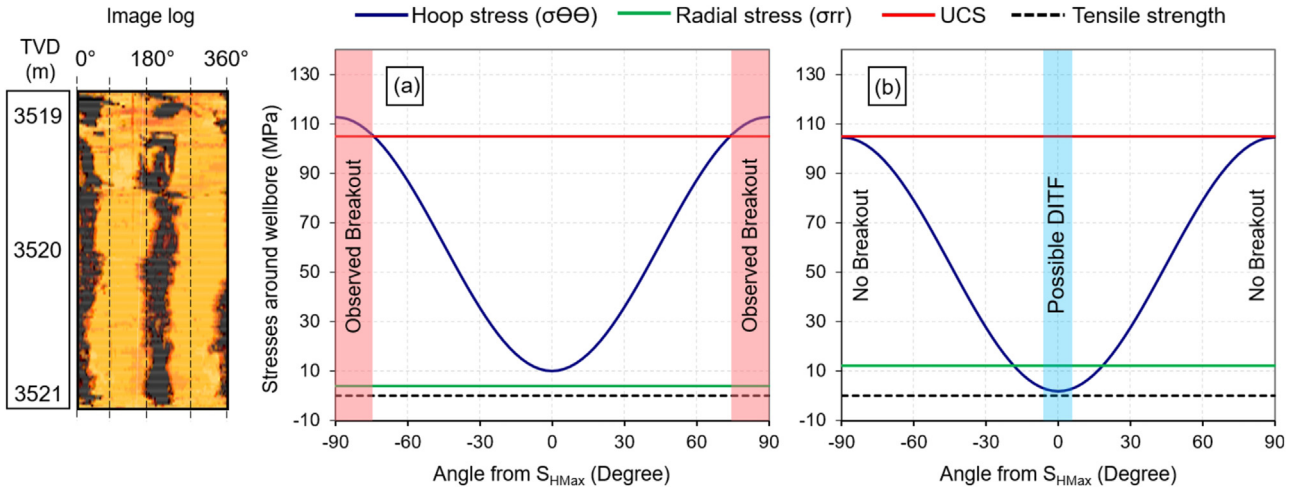


**Fig. 16.** Distribution of stresses at the borehole wall and associated failures in the Ordovician reservoir (3520 m), Well-E. (a) represents the drilling condition with 52 MPa drilling fluid pressure, and (b) represents the stress concentrations if drilling fluid pressure is increased to 60 MPa.

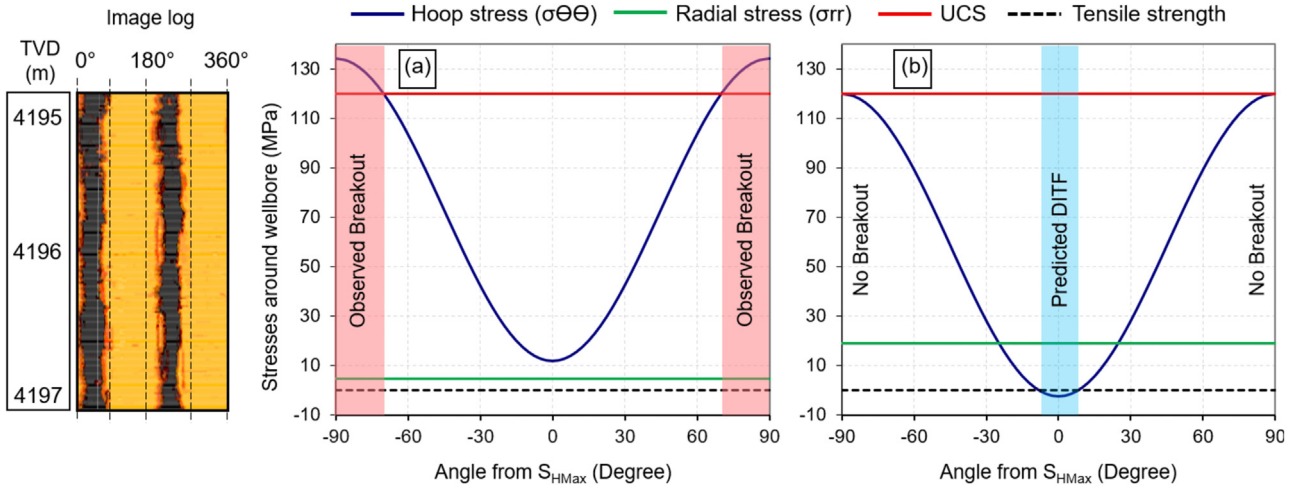


**Fig. 17.** Distribution of stresses at the borehole wall and associated failures in the Cambrian reservoir (4196 m), Well-E. (a) represents the drilling condition with 62 MPa drilling fluid pressure and (b) represents the stress concentrations if drilling fluid pressure is increased to 76 MPa.

ures (DITF) since $\sigma_{\Theta\Theta}$ was higher than $\sigma_{rr}$ (with 52 MPa mud pressure; Fig. 16a). To prevent this breakout, we found that the downhole mud pressure needs to be increased by about 8 MPa, which will be able to decrease the $\sigma_{\Theta\Theta}$ magnitude and prevent compressive failures (Fig. 16b). However, by doing so, we envisage that the borehole wall can locally go into tension with hoop stress becoming lower than the radial stress (Zoback, 2007), and DITF is, therefore likely to occur parallel to the $S_{HMax}$ orientation (Fig. 16b). The same situation has also been observed in the Cambrian reservoirs of our study area, which are more affected by compressive failures. The stress distribution at 4196 m depth in Well-E indicates extensive breakouts with 62 MPa drilling mud while DITF was absent in the image log (Fig. 17a). An increase of mud pressure by about 14 MPa will be necessary to completely avoid compressive failures with the high possibility of DITF occurrences in the Cambrian reservoir (Fig. 17b).

It is to be noted that DITF does not propagate longer from the borehole wall into the fresh formation (usually less than 1 cm; Brudy and Zoback, 1999) and therefore does not have a considerable effect on the wellbore stability while drilling compared to the breakouts, which are associated with significant borehole overgauging. However, the decision of increasing the mud pressure to prevent BO should be carefully considered. If the revised mud pressure exceeds the $S_{hmin}$ gradient, DITF may result in a hydraulic fracture propagating away from the borehole through which a significant amount of drilling fluid can be lost within the reservoir. This mud loss or lost circulation events intensify the operational complexity during drilling as the mitigation techniques increase cost (material cost as well as rig standby cost) considerably. This also has critical implications for near-wellbore reservoir damage as it can significantly reduce the formation permeability around the wellbore, and the success of perforation can be compromised in a highly overgauged hole (higher cement thickness between casing and formation).

### 7.4. Reservoir stimulation and associated fracture reactivations risks

Artificial reservoir stimulation treatments are necessary to boost the hydraulic properties and enhance hydrocarbon production from these tight formations. The success of hydraulic fracturing is very much dependent on reservoir continuity which has the lowest risk possibility in the case of the studied Paleozoic reservoirs in the Oued Mya due to their widespread geological continuation across the field. Hydrofracking horizontal wells in these tight and thick reservoir units are more attractive and fruitful compared to multilateral completions (Shehata et al., 2010). Going by the thickness and continuity of the studied reservoirs, a very close analog for stimulation design can be the L12/L15

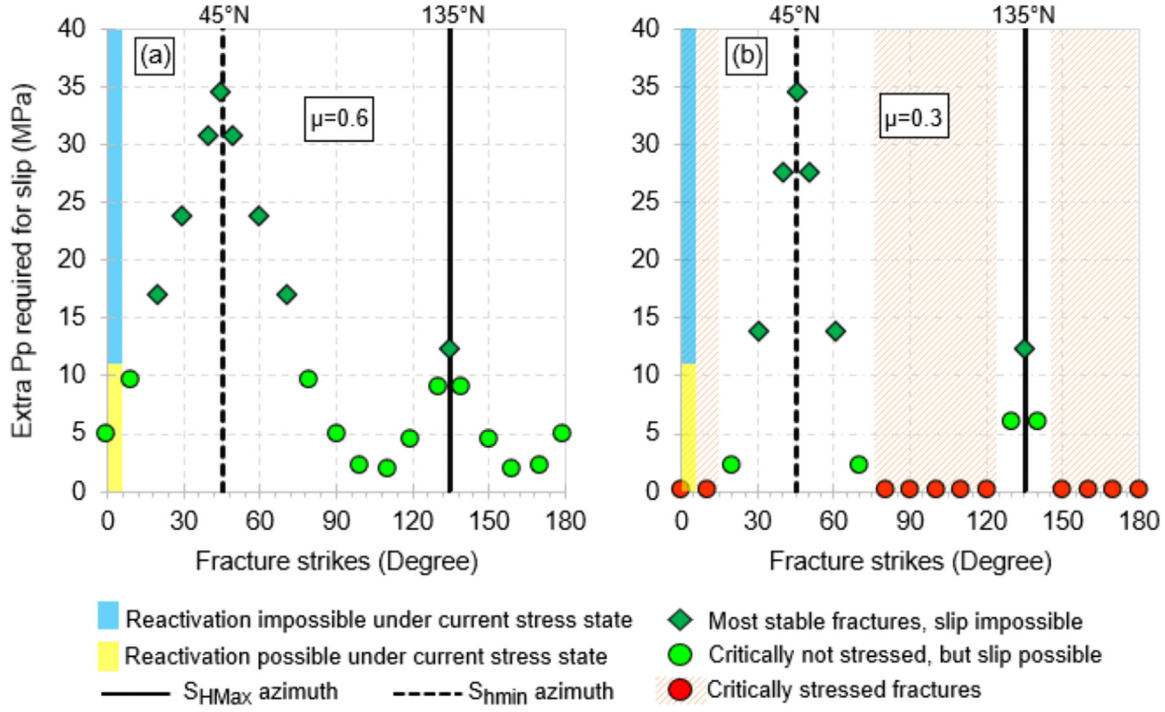


**Fig. 18.** Fracture reactivation potential during hydraulic fracturing at reservoir level considering (a) μ = 0.6 and (b) μ = 0.3 (weak fracture planes). This analysis assumes $S_{hmin}$ and $S_{HMax}$ gradients as 17.3 and 23.8 MPa/km respectively with mean $S_{HMax}$ orientation as 135°N.

field of the southern North Sea, the offshore Netherlands, where Weijermans et al. (2016) reported the full reservoir coverage with a single fracture of 110 m height and 130 m width. A similar design can be achieved with a 2-5 m perforation interval in the middle of the reservoir interval. We recommend applying hydro-jetting with coil tubing to get the maximum benefit of perforation, as this results in larger perforation paths. The absence of considerable natural fractures within the reservoirs excludes the risk associated with near-wellbore tortuosity and screens out problems (Cleary et al., 1993). To achieve an optimum completion, the horizontal well trajectories should be parallel to the field $S_{hmin}$ orientation (NE-SW). With the $S_{hmin}$ parallel well path, oriented perforations aligned along the $S_{HMax}$ direction will provide better fracture connectivity and induced permeability, as hydraulic fractures propagate parallel to the $S_{HMax}$.

Reservoir pressurization during hydrofracking increases the acting fluid pore pressure and thus reduces the effective stress magnitudes. This can lead to shear slippage on optimally oriented faults at reservoir levels. Based on the interpreted in-situ stress gradients and horizontal stress orientations, we anticipated and quantified the extra pore pressure required by fractures to experience slip during stimulation, as depicted in Fig. 18. Friction on the faults and fractures is an important controlling parameter in this analysis. Studies indicate that the frictional coefficient (μ) ranges between 0.6-0.85 (Scholz, 2000; Zoback, 2007). Considering μ = 0.6, our results (Fig. 18a) implied that a minimum of 2.1 MPa pore pressure increase will be required for a slip to happen, however, at the present stress state, none of the fractures are critically stressed. We also identified the most stable fracture orientations (with no-slip) based on the fact that critical pore pressure buildup will not exceed the reservoir $S_{hmin}$ magnitude during the fracking process.

However, the assumption of μ = 0.6 may underestimate the potential weak fracture planes, which are comparatively more vulnerable. Clay-rich gouge material can make the fractures extremely weak. Ikari et al. (2009) suggested the frictional properties of illite and chlorite-rich fault gouge to be associated with $\mu$ ranges within 0.27 to 0.32. Based on the petrophysical analysis, Chlorite and Illite are the principal clay minerals present within the Cambrian and Ordovician reservoirs respectively, which led us to infer the fracture slippage analysis assuming $\mu = 0.3$ (Fig. 18b). With decreased frictional strength a majority of the fracture orientations are observed to be critically stressed and do not offer any repressurization window. From the analysis, it is found that the faults and fractures striking N30°E- N60°E are the most stable ones with potentially no risk of slippage during stimulation. However, this analysis is based on the mean $S_{HMax}$ azimuth of N135°E. We observed minor deflection in the horizontal stress azimuth in the region, and it varies between N125°E and N135°E, as seen in the image logs of the six studied wells. Therefore, considering an overall NW-SE $S_{HMax}$ orientation, the N-S and E-W trending weak planes (faults, fractures) possess the highest shear slippage vulnerability during fluid repressurization. Since the frictional measurement data is unavailable, we recommend the seismic data analysis to delineate the fault plane orientations cutting through the Paleozoic reservoirs, which can then be compared with the interpreted fracture trends that have more slip vulnerability during stimulation.

### 7.5. Associated uncertainties and model limitations

The geomechanical workflows followed in the oil and gas industry are primarily based on the wireline logs and require direct measurements for calibration and validation. However, such measurements are scarce, which introduces uncertainties in the outputs. Literature survey and offset field data analysis can help to gain some confidence, but the key is to integrate all possible information to extract the maximum possible information. For example, based on the spectral gamma-ray data, we inferred the reservoir mineralogy is clay-dominated. The XRD data of the same reservoir intervals from the nearby southern Hassi Messaoud field also reports illite and chlorite as dominant clay minerals plugging the reservoir pore spaces (Benayad et al., 2014), which supports our

inference. It is to be noted that the clay mineralogy is best understood by XRD data and spectral gamma ray-based mineralogy identification is an indirect interpretation (De and Sengupta, 2021; Kala et al., 2021) that may have uncertainties due to the lateral heterogeneity of the reservoir facies. We have utilized RQI and FZI to infer reservoir quality, however, these methods need to be calibrated with static and dynamic fluid flow parameters, which was beyond the scope of the present work.

In this work, we utilized Eaton's uniaxial strain model to estimate the $S_{hmin}$ magnitude. This is a very simplistic approach and some recent works argued that this method provides the $S_{hmin}$ lower bound (Zhang and Zhang, 2017; Zhang et al., 2021). We interpreted a 17.30-19.20 MPa/km gradient range of reservoir $Sh_{min}$ from the minifrac (Fig. 8) and the calculated $S_{hmin}$ profile (using Eq. 2) shows that it mostly follows the minifrac lower bound (Fig. 9). It is very difficult to satisfy all minifrac data by a single $S_{hmin}$ profile in any well. Therefore, we presented upper and lower bounds of minimum horizontal stress following Mathews and Kelly's approach which is represented by an effective minimum horizontal stress ratio ranging between 0.53 and 0.64. However, it is critical to mention that only six such calibration data point from a single well is not enough to provide a confident validation and sufficient statistical coverage when used in MLR models. Although the availability of direct downhole measurements had always been a concern and offers critical challenges in subsurface geomechanical calibration. The only published $S_{hmin}$ measurements of the Paleozoic reservoirs were available from English et al. (2017), who reported a 12.7-23.4 MPa/km $S_{hmin}$ gradient range in the Illizi Basin from various downhole injection tests (minifrac, step-rate test, etc.). Our inferred $S_{hmin}$ gradient comfortably falls within the reported range. We had Leak-off test (LOT) data available at casing shoe depths, recorded in shales, much above the reservoirs. Based on our regional experiences and published pieces of literature, we have observed that LOT data is easier to get and commonly utilized to validate a calculated $S_{hmin}$ profile of the entire stratigraphy within a single well. Since minimum horizontal stress is sensitive to lithological variations and our study intends to focus only on the reservoirs, we preferred not to use those LOT values to infer and model reservoir $S_{hmin}$.

Maximum horizontal stress magnitude estimation is the most challenging aspect of any geomechanical modeling. There are several methods available to estimate $S_{HMax}$, each comes with certain limitations. In this study, we have employed the two most extensively used approaches to infer $S_{HMax}$ magnitude. In the first approach, we interpreted the breakout widths from the acoustic image logs and used the same to calculate $S_{HMax}$ magnitude (Barton et al., 1988; Zoback, 2007). Referring to the input parameters of Eq. (5), it is to be noted that breakout-derived $S_{HMax}$ output will have uncertainties contributed by $S_{hmin}$ and UCS. We have already discussed the $S_{hmin}$ estimates, which are often calibrated with minifrac measurements. We did not have any direct core-based UCS measurements, and therefore it majorly contributes to the $S_{HMax}$ uncertainty. In this regard, we refer to the work published by English et al. (2017), where the UCS range of 90.38-191.02 MPa is presented based on the core measurements of the Ordovician reservoirs from the Illizi Basin, southeastern Algeria. Our log-based UCS estimate varies between 95 MPa and 150 MPa, which is well within the published range, yet the uncertainty remains due to the lack of measured data. One of the major issues with the accuracy of the breakout width-based method is the time-dependent breakout deepening (Zoback, et al., 1985). Stress re-distribution induced by rock failure and plastic deformation causes the change in compressive stress at the breakout tip. As time goes by, the rock at the breakout tip may fail and advance due to accumulated stress concentration. The breakout measurement usually takes place at least after a few hours of drilling, which means the depth measured is deeper than initially formed. In this case, the stress calculation based on elastic conditions yields unreliable results. Thereby, pre-existing fractures around the borehole can also result in the elongation of a breakout, which further disrupts the estimation.

Other than that, breakouts have to exist to allow the stress measurement to take place and a continuous breakout rarely occurs within a single formation. An in-depth wellbore stability analysis and optimum downhole drilling mud are capable of reducing or even avoiding compressive failures. Also, image logs are expensive and do not usually run in all the wells. In such situations, the breakout width-based method is inapplicable. This leads us to employ the second approach, where we followed the poroelastic strain model. This model requires the horizontal strains, which are dependent on the core-measured static Poisson's ratio and Young's modulus. Wang (2000) suggested that the static and dynamic Poisson's ratios are almost equal to each other, which is also extensively followed by various researchers for stress analysis. On the other hand, there are many published relationships between the static and dynamic Young's modulus (Yale, 1994; Brotons et al., 2016; Fjær, 2019). However, none of them are reported from the Paleozoic reservoirs of the Algerian Sahara. In absence of the core-measured rock-mechanical data, we had used the log-derived Young's modulus, which might have overestimated the $S_{HMax}$. We avoided using any published static to dynamic Young's modulus transform since there is no way to confirm the applicability of the same in our studied reservoir. However, based on the limited $S_{hmin}$ measurements, the stress polygon analysis (Fig. 15) provided a reasonable $S_{HMax}$ range using the breakout criteria and confidently infers the reservoir stress state as a strike-slip regime.

Since both the $S_{HMax}$ approaches have certain limitations, we engaged the MLR model to establish a fitting $S_{HMax}$ equation with key controlling variables. This suggests how a predictor variable may be quantitatively related to the estimated horizontal stress magnitudes and can help to formulate an objective function to achieve a suitable model. Since the log-derived UCS falls within the published core-measured ranges of the offset field, we compared our MLR-generated output with the breakout width-based $S_{HMax}$. The established MLR model is a simple yet powerful method to provide reasonable estimates of the outcome variables, i.e., horizontal stress magnitudes (both $S_{hmin}$ and $S_{HMax}$) for the studied field. Nevertheless, the application of the developed model for other fields, especially reservoirs with complex structural features, may still have some restrictions and certainly need a specific model that explains the data suitably. The established model can be updated for more accurate estimates if more measured data or training samples are introduced, which is beyond the scope of this study.

## 8. Conclusions

Oued Mya Basin hosts a large volume of sub-millidarcy reservoir intervals in the Paleozoic succession. The successful drilling and completion of these tight oil reservoirs are critically important for the project delivery and its economics. We have addressed these by well-based geomechanical modeling presented in this work. This is a first of its kind to report the comprehensive stress state interpretations from the deep Paleozoic reservoirs of the Oued Mya Basin, northeastern Algerian Sahara. For this, the geophysical logs and direct downhole measurements were integrated to get insights into the reservoir's stress state. Due to the lack of core-based rock-mechanical measurements and sufficient downhole calibration data, we employed multiple approaches to address the in-situ stress distribution. Two newly established statistical regression models with excellent goodness of fit values ($R^2$ = 0.976 and 0.994) have been proposed to predict horizontal stress magnitudes. The MLR-predicted $S_{hmin}$ and $S_{HMax}$ magnitudes are found

to be in good agreement with minifrac measurements and breakout width-based stress estimates for the studied wells, including the wells that were used to validate the model and not during the multiple regression analyses. The sensitivity of the $S_{HMax}$ magnitudes due to the influencing parameters such as $P_p$, $S_v$, $S_{hmin}$, $\upsilon$, and $E$ have been studied and their relative importance is discussed accordingly. In practice, image logs and downhole calibration data are scarce, which are also critical for inferring reservoir stresses and optimum field development programs. The newly proposed $S_{HMax}$ and $S_{hmin}$ equations, thus are significant contributions, as these can be utilized in absence of validation parameters in the studied region. The same can be highly applicable for Paleozoic reservoirs in the other Algerian hydrocarbon fields that follow similar structural configurations. Based on the interpreted pore pressure and in-stress distribution, we recommended optimum drilling and reservoir development strategies to avoid wellbore instability and fracture reactivation risks during stimulation.

## Declaration of Competing Interest

The authors declare that they have no known competing financial interests or personal relationships that could have appeared to influence the work reported in this paper.

## CRediT authorship contribution statement

**Rafik Baouche:** Data curation, Supervision, Project administration, Resources, Formal analysis, Writing – review & editing. **Shib Sankar Ganguli:** Conceptualization, Resources, Formal analysis, Methodology, Validation, Visualization, Writing – original draft, Writing – review & editing. **Souvik Sen:** Conceptualization, Resources, Formal analysis, Methodology, Validation, Visualization, Writing – original draft, Writing – review & editing. **Ahmed E. Radwan:** Resources, Writing – review & editing.

## Acknowledgments

We are grateful to Chengxue Yang (Editorial Secretary) and Dr. Yirang Jang (Associate Editor) for careful editorial handling, and the anonymous reviewers for their critical comments. We express our sincere thanks to Amerada Hess Algeria and SONATRACH for providing the dataset and technical reports. R. Baouche thanks the Laboratory of Resources Minérals at Energétiques, University of Boumerdes, and the Directorate General for Scientific Research and Technological Development (DG-RSDT) of the Ministry of Higher Education and Scientific Research of Algeria for supporting this research works. SSG would like to thank Director, CSIR-NGRI for providing permission to conduct and publish the results. SSG offers deep gratitude to the DST Inspire Faculty project for funding support.

## References

Abuamarah, B.A., Nabawy, B.S., 2021. A proposed classification for the reservoir quality assessment of hydrocarbon-bearing sandstone and carbonate reservoirs: a correlative study based on different assessment petrophysical procedures. J. Nat. Gas Sci. Eng. 88, 103807.

Abuamarah, B.A., Nabawy, B.S., Shehata, A.M., Kassem, O.M.K., Ghrefat, H., 2019. Integrated geological and petrophysical characterization of Oligocene deep marine unconventional poor to tight sandstone gas reservoir. Mar. Petrol. Geol. 109, 868–885.

Amaefule, J., Altunbay, M., Tiab, D., Kersey, D., Keelan, D., 1993. Enhanced reservoir description, using core and log data to identify hydraulic (flow) units and predict permeability in uncored intervals/wells. In: Proc. SPE Annual Technical Conference and Exhibition, Houston, Texas. SPE 26436.

Baouche, R., Sen, S., Chaouchi, R., Ganguli, S.S., 2021a. Modeling In-situ tectonic stress state and maximum horizontal stress azimuth in the Central Algerian Sahara – a geomechanical study from El Agreb, El Gassi and Hassi Messaoud fields. J. Natur. Gas Sci. Eng. 88, 103831. doi:10.1016/j.jngse.2021.103831.

Baouche, R., Sen, S., Chaouchi, R., Ganguli, S.S., 2021b. Modeling in-situ tectonic stress state and maximum horizontal stress azimuth in the Central Algerian Sahara – A geomechanical study from EL Agreb, EL Gassi and Hassi Messaoud fields. J. Natur. Gas Sci. Eng. 88, 103831. doi:10.1016/j.jngse.2021.103831.

Baouche, R., Sen, S., Ganguli, S.S., Boutaleb, K., 2021c. Petrophysical and geomechanical characterization of the Late Cretaceous limestone reservoirs from the Southeastern Constantine Basin, Algeria. Interpretation (SEG) 9 (4). doi:10.1190/int-2020-0249.1.

Baouche, R., Sen, S., Boutaleb, K., 2020a. Present day In-situ stress magnitude and orientation of horizontal stress components in the eastern Illizi basin, Algeria: a geomechanical modeling. J. Struct. Geol. 132, 103975.

Baouche, R., Sen, S., Boutaleb, K., 2020b. Distribution of pore pressure and fracture pressure gradients in the Paleozoic sediments of Takouazet field, Illizi basin, Algeria. J. Afr. Earth Sci. 164, 103778.

Baouche, R., Sen, S., Ganguli, 2020c. Pore pressure and in-situ stress magnitudes in the Bhiret Hammou hydrocarbon field, Berkine Basin, Algeria. J. Afr. Earth Sci. 171, 103945.

Barton, C.A., Zoback, M.D., Burns, K.L., 1988. In-situ stress orientation and magnitude at the Fenton Geothermal Site, New Mexico, determined from wellbore breakouts. Geophys. Res. Lett. 15, 467–470.

Barton, C., Moos, D., 2010. Geomechanical wellbore imaging: key to managing the asset life cycle. In: Poppelreiter, M., Garcia-Carballido, C., Kraaijveld, M. (Eds.), Dipmeter and Borehole Image Log Technology. AAPG Memoir 92. American Association of Petroleum Geologists, pp. 81–112.

Benamrane, O., Messaoudi, M., Messelles, H., 1993. Geology and hydrocarbon potential of the Oued Mya Basin, Algeria. In: Proc. AAPG International Conference and Exhibition, The Netherlands, AAPG Search and Discovery Article #90990.

Benayad, S., Park, Y.S., Chaouchi, R., Kherfi, N., 2014. Parameters controlling the quality of the Hamra Quartzite reservoir, southern Hassi Messaoud, Algeria: insights from a petrographic, geochemical and provenance study. Arabian J. Geosci. 7, 1541–1557.

Benayad, S., Park, Y.S., Chaouchi, R., Kharfi, N., 2013. Unconventional resources in Algeria: appraisal result from the Hamra Quartzite reservoir. GeoSci. Jour. 17, 313–327.

Benayad, S., Park, Y.S., Kharfi, N., 2011. The hamra quartzite tight reservoir properties in the Oued Mya Basin, Algeria. In: Proc. 73rd EAGE Conference and Exhibition incorporating SPE EUROPEC, Vienna, Austria doi:10.3997/2214-4609.20149703.

Boote, D.R.D., Clark-Lowes, D.D., Traut, M.W., 1998. Palaeozoic petroleum systems of North Africa. In: Macgregor, D.S., Moody, R.T.J., Clark-Lowes, D.D. (Eds.), Petroleum geology of North Africa, Geological Society. Special Publication 132, London, pp. 7–68.

Brotons, V., Tomas, R., Ivorra, S., Grediaga, A., Martinez-Martinez, J., Benavente, D., Gomez-Heras, M., 2016. Improved correlation between the static and dynamic elastic modulus of different types of rocks. Mater. Struct. 49, 3021–3037.

Brudy, M., Zoback, M.D., 1999. Drilling-induced tensile wall-fractures: implications for the determination of in situ stress orientation and magnitude. Int. J. Rock Mech. Min. Sc. 136, 191–215.

Busetti, S., Reches, Z.E., 2014. Geomechanics of hydraulic fracturing microseismicity: Part 2, Stress state determination. AAPG Bull. 98 (11), 2459–2476.

Carr, I.D., 2002. Second order sequence stratigraphy of the Paleozoic of North Africa. J. Petrol. Geol. 25, 259–280.

Cleary, M.P., Johnson, D.E., Kogsbøll, H.-H., Owens, K.A., Perry, K.F., de Pater, C.J., Stachel, A., Schmidt, H., Mauro, T., 1993. Field implementation of proppant slugs to avoid premature screen-out of hydraulic fractures with adequate proppant concentration. In: Proc. Low Permeability Reservoirs Symposium, Denver, Colorado, Apr 26-28. SPE-25892.

De, S., Aastha, Sengupta, D., 2020. Depositional environment and geomechanical properties of ambay Shale: potential reservoir for shale oil and gas in India. Arabian J. Geosci. 13 (12), 1–12.

De, S., Sengupta, D., 2021. Evaluating the geomechanical properties of Cambay Shale, Cambay Basin, India using advanced wireline logs for shale hydrocarbon exploration. Pet. Sci. Technol. 39 (11-12), 392–409.

Di Bucci, D., Burrato, P., Vannoli, P., Valensise, G., 2010. Tectonic evidence for the ongoing Africa-Eurasia convergence in central Mediterranean foreland areas: A journey among long-lived shear zones, large earthquakes, and elusive fault motions. J. Geophys. Res. 115, B12404. ttps://www.eni.com/en-IT/eni-worldwide/africa/algeria.html.

English, J.M., Finkbeiner, T., English, K.L., Cherif, R.Y., 2017. State of Stress in Exhumed Basins and Implications for Fluid Flow: Insights from the Illizi Basin, Algeria. Geol. Soc. London 458, 89–112 Special Publications.

Eschard, R., Hussein, A., Braik, F., Desaubliaux, G., 2005. The Lower Paleozoic succession in the Tassili outcrops, Algeria: sedimentology and sequence stratigraphy. First Break 23, 27–36.

Fjær, E., 2019. Relations between static and dynamic moduli of sedimentary rocks. Geophys. Prospect. 67, 128–139.

Freyburg, E., 1972. Der untere trod mittlere Buntsandstein SW-Thiiringens in seinen gesteinstechnischen Eigenschatten. Ber. Dte. Ges. Geol. Wiss A 17, 911–919.

Galeazzi, S., Point, O., Haddadi, N., Mather, J., Druesne, D., 2010. Regional geology and petroleum systems of the Illizi-Berkine area of the Algerian Saharan Platform: an overview. Marine Petrol. Geol. 27, 143–178.

Ganguli, S.S., Sen, S., 2020. Investigation of present-day in-situ stresses and pore pressure in the south Cambay Basin, western India: Implications for drilling, reservoir development and fault reactivation. Mar. Petrol. Geol. 118, 104422. doi:10.1016/j.marpetgeo.2020.104422.

Gholami, R., Moradzadeh, A., Rasouli, V., Hanachi, J., 2014. Practical application of failure criteria in determining safe mud weight windows in drilling operations. J. Rock Mech. Geotech. Eng. 6 (1), 13–25.
Hirst, J.P.P., Davis, N., Palmer, A.F., Achache, D., Riddiford, F.A., 2001. The 'tight gas' challenge: appraisal results from the Devonian of Algeria. Petrol. Geosc. 7 (1), 13–21.
Heidbach, O., Rajabi, M., Cui, X., Fuchs, K., Müller, B., Reinecker, J., Reiter, K., Tingay, M., Wenzel, F., Xie, F., Ziegler, M.O., Zoback, M.L., Zoback, M.D., 2018. The World Stress Map database release 2016: crustal stress pattern across scales. Tectonophy 744, 484–498.
Ikari, M.J., Saffer, D.M., Marone, C., 2009. Frictional and hydrologic properties of clay-rich fault gouge. J. Geophys. Res. 114 (B5). doi:10.1029/2008JB006089.
Javani, D., Aadnoy, B., Rastegarnia, M., Nadimi, S., Aghighi, M.A., Maleki, B., 2017. Failure criterion effect on solid production and selection of completion solution. J. Rock Mech. Eng. Geotech. Eng. 9, 1123–1130.
Ju, W., Shen, J., Qin, Y., Meng, S.Z., Wu, C.F., Shen, Y.L., Yang, Z.B., Li, G.Z., Li, C., 2017. In-situ stress state in the Linxing region, eastern Ordos Basin, China: implications for unconventional gas exploration and production. Mar. Petrol. Geol. 86, 66–78.
Kala, S., Devaraju, J., De, S., Rasheed, M.A., 2022. Multiproxy geochemical characterization of Kommugudem Formation, Krishna Godavari Basin, India: Implication on hydrocarbon potential and Shale brittleness. Geol. J. 57 (4), 1373–1390.
Kassem, A.A., Sen, S., Radwan, A.E., Abdelghany, W.K., Abioui, M., 2021. Effect of depletion and fluid injection in the mesozoic and paleozoic sandstone reservoirs of the october oil field, Central Gulf of Suez Basin: implications on drilling, production and reservoir stability. Nat. Res. Res. 30, 2587–2606.
Klaja, J., Dudek, L., 2016. Geological interpretation of spectral gamma ray (SGR) logging in selected boreholes. Nafta-Gaz 72.
Klett, T.R., 2000. Total Petroleum Systems of the Trias/Ghadames Province, Algeria, Tunisia, and Libya-The Tanezzuft-Oued Mya, Tanezzuft-Melrhir, and Tanezzuft-Ghadames. U.S. Geol. Survey Bull., 2202-C. KeyFacts Energy, 201. 6. https://www.keyfactsenergy.com/media/country_review/Algeria_PVh46GI.pdf.
Kneller, B.C., Branney, M.J., 1995. Sustained high density turbidity currents and the deposition of thick massive sands. Sedimentology 42, 607–616.
Koceir, M., Tiab, D., 2000. Influence of stress and lithology on hydraulic fracturing in Hassi Messaoud Reservoir, Algeria. In: Proc. SPE/AAPG Western Regional Meeting, Long Beach, CA, USA. June 19-22, SPE-62608-MS.
Lai, J., Wang, G., Wang, S., Cao, J., Li, M., Pang, X., Han, C., Fan, X., Yang, L., He, Z., Qin, Z., 2018. A review on the applications of image logs in structural analysis and sedimentary characterization. Mar. Petrol. Geol. 95, 139–166.
Lang, J., Dixon, R.J., Le Heron, D.P., Winsemann, J., 2012. Depositional architecture and sequence stratigraphic correlation of Upper Ordovician glaciogenic deposits, Illizi Basin. Algeria. Geol. Soc. London Spec. Publ. 368, 293–317.
Liang, M., Peng, S., Du, W., Lu, Y., 2018. Tectonic stress estimation from ultrasonic borehole image logs in a coal bed methane well, northeastern Qinshui Basin, China. J. Nat. Gas Sc. Eng. 52, 44–58.
Liu, S., Harpalani, S., 2014. Evaluation of in situ stress changes with gas depletion of coalbed methane reservoirs. J. Geophys. Res. Solid Earth 119, 6263–6276.
Lockner, D.A., 1995. Rock Failure. Rock physics and phase relations. In: Proc. American Geophysical Union, Washington, D.C, pp. 127–147.
Lund Snee, J., Zoback, M.D., 2020. Multiscale variations of the crustal stress field throughout North America. Nat. Comm. 11, 1951.
Matthews, W.R., Kelly, J., 1967. How to predict formation pressure and fracture gradient. Oil Gas J 65 (8), 92–106.
McDougall, N.D., Braik, F., Clarke, P., Kaced, M., 2003. The Upper Ordovician of the Illizi Basin, Algeria: a core-based study of Unit IV Palaeovalleys. AAPG Hedberg Conference: Paleozoic and Triassic Petroleum Systems in North Africa, Algiers.
McGowen, J.M., Benani, A., Ziada, A., 1996. Increasing oil production by hydraulic fracturing in the Hassi Messaoud Cambrian Formation, Algeria. In: Proc. SPE European Petroleum Conference, Italy, SPE-36904-MS.
Morley, C.K., 2010. Stress re-orientation along zones of weak fabrics in rifts: an explanation for pure extension in 'oblique' rift segments? Earth Planet. Sci. Lett. 297 (3-4), 667–673.
Mulder, T., Alexander, J., 2001. The physical character of subaqueous sedimentary density flows and their deposits. Sedimentology 48, 269–299.
Najibi, A.R., Ghafoori, M., Lashkaripour, G.R., Asef, M.R., 2017. Reservoir geomechanical modeling: In-situ stress, pore pressure, and mud design. J. Petrol. Sc. Eng. 151, 31–39. doi:10.1016/j.petrol.2017.01.045.
Nabawy, B.S., Rashed, M.A., Mansour, A.S., Afify, W.S.M., 2018. Petrophysical and microfacies analysis as a tool for reservoir rock typing and modeling: Rudeis Formation, offshore October Oil Field, Sinai. Mar. Pet. Geol. 97, 260–276.
Paludan, J., Kerrouche, N., Toufik, H., Belahmeur, S., 2017. The state of stress in North Africa - a conceptual model based on borehole image data from Algerian Oil Wells. In: Proc. Second EAGE Borehole Geology Workshop doi:10.3997/2214-4609.201702381.
Parvizi, H., Rezaei-Gomari, S., Nabhani, F., Turner, A., Feng, W.C., 2015. Hydraulic fracturing performance evaluation in tight sand gas reservoirs with high perm streaks and natural fractures. In: Proc. EUROPEC, Madrid, Spain, June 1-4, SPE-174338.
Patton, T.L., Batchelor, A.S., Foxford, K.A., Hellman, T.J., Maache, N., 2003. In situ stress state – Tiguentourine Field, southeastern Algeria. In: Proc. AAPG Hedberg Conference, Paleozoic and Triassic Petroleum Systems in North Africa, Algeria.
Petroconsultants, 1996a. Petroleum exploration and production database. Petroconsultants, Inc., Houston, Texas [database available from Petroconsultants, Inc., P.O. Box 740619, Houston, TX 77274-0619].
Plumb, R.A., Evans, K.F., Engelder, T., 1991. Geophysical log responses and their correlation with bed to bed stress contrasts in Paleozoic rocks, Appalachian plateau, New York. J. Geophys. Res. 96 (B9), 14509–14528. doi:10.1029/91JB00896.
Radwan, A., Sen, S., 2021a. Stress path analysis for characterization of in situ stress state and effect of reservoir depletion on present-day stress magnitudes: reservoir geomechanical modeling in the Gulf of Suez rift basin. Egypt. Nat. Resour. Res. 30, 463–478.
Radwan, A.E., Sen, S., 2021b. Characterization of in-situ stresses and its implications for production and reservoir stability in the depleted El Morgan hydrocarbon field, Gulf of Suez rift basin. Egypt. J. Struct. Geol. 148, 104355.
Rajabi, M., Tingay, M., Heidbach, O., 2016. The present-day state of tectonic stress in the Darling Basin, Australia: implications for exploration and production. Mar. Petrol. Geol. 77, 776–790. doi:10.1016/j.marpetgeo.2016.07.021.
Scholz, C.H., 2000. Evidence for a strong San Andreas fault. Geology 28 (2), 163–166.
Shehata, A., Aly, A., Ramsey, L., 2010. Overview of tight gas field development in the Middle East and North Africa region. In: Proc. SPE North Africa Technical Conference and Exhibition, Cairo, Egypt, Feb 14-17, SPE-126181.
Sohail, G.M., Hawkes, C.D., Yasin, Q., 2020. An integrated petrophysical and geomechanical characterization of Sembar Shale in the Lower Indus Basin, Pakistan, using well logs and seismic data. J. Nat. Gas Sci. Eng. 78, 103327.
Stow, D.A.V., Johansson, M., 2000. Deep-water massive sand: nature, origin and hydrocarbon implications. Mar. Petrol. Geol. 17, 145–174.
Tingay, M., Morley, C., Hillis, R.R., Meyer, J.J., 2010. Present-day stress orientation in Thailand's basins. J. Struct. Geol. 32, 235–248.
Tingay, M.R., Hillis, R.R., Morley, C.K., King, R.C., Swarbrick, R.E., Damit, A.R., 2009. Present-day stress and neotectonics of Brunei: implications for petroleum exploration and production. AAPG Bull. 93, 75–100.
Taghipour, M., Ghafoori, M., Lashkaripour, G.R., Moghaddas, N.H., Molaghab, A., 2019. Estimation of the current stress field and fault reactivation analysis in the Asmari reservoir. SW Iran. Petrol. Sci. 16, 513–526.
Wang, H.F., 2000. Theory of Linear Poroelasticity with Applications to Geomechanics and Hydrogeology. Princeton University Press, p. 304.
Weijermns, P., Daniau, G., Westerhof, D., 2016. Developing marginal near-tight gas fields in a mature area with long-reach hydraulically fractured wells – A case study. In: Proc. SPE Europec, 78th EAGE Conference and Exhibition, Vienna, Austria, May 30- June 2, SPE-180169.
Yahi, N., Khatir, B., 1993. Source rock identification and basin modelling Mouydir /Oued Mya Basin, Central Algeria doi:10.3997/2214-4609.201409701.
Yale, D.O., 1994. Static and dynamic rock mechanical properties in the Hugoton and Panoma fields, Kansas. In: Proc. SPE Mid-Continent Gas Symposium, Amarillo, Texas, May 22-24. SPE-27939.
Zhang, Y., Yin, S., Zhang, J., 2021. In situ stress prediction in subsurface rocks: an overview and a new method. Geofluids 6639793.
Zhang, Y., Zhang, J., 2017. Lithology-dependent minimum horizontal stress and in-situ stress estimate. Tectonophysics 703-704, 1–8.
Zhang, J., 2013. Borehole stability analysis accounting for anisotropies in drilling to weak bedding planes. Intl. J. Rock Mech. Min. Sc. 60, 160–170.
Zoback, M.D., 2007. Reservoir Geomechanics. Cambridge Univ. Press.
Zoback, M D, Moos, D, Mastin, L., Anderson, R N, 1985. Well bore breakouts and in situ stress. JGR 5523–5530.